



Contents lists available at ScienceDirect

Journal of Asian Earth Sciences

journal homepage: www.elsevier.com/locate/jseas

Geochronology, geochemistry and tectonic implications of Late Triassic granites in the Mongolian Altai Mountains



Batulzii Dash^a, Enkhjargal Boldbaatar^a, Oyun-Erdene Zorigtkhuu^a, An Yin^{b,c,*}

^a Department of Geology, School of Geology and Petroleum Engineering, Mongolian University of Science and Technology, P.O. 46/654, Ulaanbaatar 210646, Mongolia

^b Department of Earth, Planetary, and Space Sciences, University of California Los Angeles, CA 90095 1567, USA

^c Structural Geology Group, China University of Geosciences (Beijing), Beijing 100085, China

ARTICLE INFO

Article history:

Received 28 November 2014
Received in revised form 24 November 2015
Accepted 24 November 2015
Available online 26 November 2015

Keywords:

Anatexis
Intracontinental subduction
Mongolian Altai
Bulgan thrust
Bodonch metamorphic complex

ABSTRACT

Although the closure of the Paleo-Asian Ocean in western China and western Mongolia occurred in the Late Carboniferous and Early Permian, widespread intra-continental magmatism continued to occur across this region from the Late Permian to the end of the Triassic. In this study we document field relationships and geochemical characterization of a Late Triassic felsic intrusive complex in the western Mongolian Altai. The plutonic complex occurs as sills, dikes, and small stocks and its composition varies from biotite granite, two-mica granite, to leucogranite. Structurally, the plutonic complex occurs in the hanging wall of a segment of the regionally extensively (>1500 km long) Irtysh–Ertix–Bulgan thrust zone. As the plutonic bodies both cut and are deformed by the shear fabrics in this regional thrust shear zone, the duration of felsic magmatism and regional thrusting was temporally overlapping. This suggests that magmatism was coeval with crustal thickening. Major- and trace-element data and isotopic analysis of granitoid samples from our study area indicate that the felsic intrusions were derived from partial melting of meta-sediments, with the biotite and two-mica granite generated through vapor-absent melting and the leucogranite from flux melting. Although the Mongolian Altai intrusions were clearly originated from anatexis, coeval granite in the Chinese Altai directly west of our study area in the hanging wall of the Irtysh–Ertix–Bulgan thrust was derived in part from mantle melting. To reconcile these observations, we propose a Himalayan-style intracontinental-subduction model that predicts two geologic settings for the occurrence of felsic magmatism: (1) along the intracontinental thrust zone where granite was entirely generated by anatexis and (2) in the hanging wall of the intracontinental thrust where convective removal and/or continental subduction induced mantle melting.

© 2015 Elsevier Ltd. All rights reserved.

1. Introduction

Anatexis is commonly associated with continent–continent collision, best exemplified by the occurrences of leucogranites exposed in the Cenozoic Himalayan orogen (e.g., Harrison et al., 1998; Yin and Harrison, 2000; Yin, 2006; Aikman et al., 2012; Guo and Wilson, 2012; Webb et al., 2013). Mechanisms of anatexis associated with collisional orogen include shear or radiogenic heating during crustal thickening, pressure-release melting induced by normal faulting and/or erosion, flux melting, and some combinations of these processes (Le Fort et al., 1987; England et al., 1992; Harris and Massey, 1994; Harrison et al., 1998; Huerta et al., 1998; Sylvester, 1998; Beaumont et al., 2001; Zeitler et al., 2001). Underplating of juvenile mafic crust could also lead to anatexis

(e.g., Sylvester, 1998; Li et al., 2013). The Himalayan models of leucogranite formation have been widely adopted for explaining the occurrences of leucogranites elsewhere in the world (e.g., Sepahi et al., 2007; Tartese and Boulvais, 2010; Sola et al., 2013; Li et al., 2014a). Granitoids originated from crustal anatexis generally comprise muscovite, sillimanite, cordierite, garnet, tourmaline, and andalusite (Le Fort et al., 1987). Their composition is also characteristically peraluminous with A/CNK ratios >1.1 and high K₂O contents (Barbarin, 1999). The Central Asian Orogenic System (also known as Central Asian Orogenic Belt) was commonly considered as an accretionary orogen assembled by amalgamation of a collage of oceanic arcs, deep-sea deposits, micro-continental terranes, and oceanic plateaus associated with significant production of juvenile crust (e.g., Şengör et al., 1993; Şengör and Natal'in, 1996; Han et al., 1997; Jahn et al., 2000; Badarch et al., 2002; Chen and Jahn, 2002; Windley et al., 2007; Kelty et al., 2008; Xiao et al., 2010), the detailed processes of accretionary tectonics and post-ocean closure interactions among tectonic deformation

* Corresponding author at: Department of Earth, Planetary, and Space Sciences, University of California Los Angeles, CA 90095 1567, USA.

E-mail addresses: yin@ess.ucla.edu, ayin54@gmail.com (A. Yin).

and magmatism have rarely been examined systematically using a combination of field mapping and modern analytical techniques (cf. Briggs et al., 2007, 2009). In this paper, we present new geological, geochronological, and geochemical data from a segment of the >1500-km long Permo-Triassic Irtysh–Ertix–Bulgan thrust shear zone in the Mongolian Altai Mountains (Fig. 1A and B). Our work reveals the occurrence of a suite of biotite granite, biotite–muscovite granite, and leucogranite in the hanging wall of the long-lived Permo-Triassic Irtysh–Ertix–Bulgan thrust shear zone. Among the investigated plutons, a biotite–muscovite granite sample yields a Late Triassic age at ~215 Ma. Based on the regional and field relationships, we tentatively propose that the granites in our study area were induced by anatexis during crustal thickening.

2. Geologic background of the study area

The study area is located in the southern margin of the western Mongolian Altai Mountains (Fig. 1A and B). The Mongolian Altai Mountains and its neighboring Russian Gorny Altai region were extensively mapped from 1960s to 1990s by Russian and Mongolian geologists (Beresi et al., 1964; Demin, 1990; Gansukh and Tileu, 1985; Samoizvantsev et al., 1982), which laid the foundation for structural and lithostratigraphic division of geology in our study area (e.g., Marinov, 1971; Marinov et al., 1973; Yanshin, 1978, 1989). The geology of the Mongolian Altai extends to the Chinese Altai Mountains, where the structural framework, magmatic history, and major tectonostratigraphic units are documented by several regionally based studies (e.g., He et al., 1990; Han et al., 1997; Windley et al., 2002; Laurent-Charvet et al., 2003; Wang et al., 2014).

Major rock types in the study area include: (1) Ordovician to Carboniferous turbidite sequences, low-grade metasedimentary strata, and meta-volcanic rocks deposited in an arc setting, (2) high-grade schist and gneiss, and (3) deformed and undeformed Paleozoic–Mesozoic granitoids (Fig. 1C and D) (Badarch et al., 2002). The most dominant structure in the study area is the north-dipping Bulgan thrust, which is the eastward extension of the Ertix thrust in China and the Irtysh fault in Kazakhstan (Fig. 1A and B). The continuity of the Ertix–Bulgan fault is disrupted by the Cenozoic right-slip Fuyun fault (Fig. 1B). Determining the timing and kinematics of the >1500 km Irtysh–Ertix–Bulgan thrust zone has been a central theme of testing the oblique subduction model of Şengör et al. (1993) as the fundamental mechanism of creating the Central Asian Orogenic System (also see Briggs et al., 2007, 2009).

The Bulgan thrust in our study area is reactivated in the Cenozoic and places high-grade metamorphic rocks over Quaternary alluvial-fan deposits (Cunningham et al., 1996) (Fig. 1D). As the fault links with the active Fuyun fault, its thrust kinematics is consistent with its being one of the termination structures of this right-slip fault system as postulated by Cunningham et al. (1996) and Cunningham (2005). Directly above the active Bulgan thrust is a shear zone consisting that is 100s m thick and consists of mylonitic gneiss and schist. Although we did not conduct systematic mapping, our field observations indicate that the mylonitic gneiss and schist bear down-dip stretching mineral lineation and the kinematic indicators such as asymmetric porphyroblasts and S-C fabrics all suggest a top-south sense of shear. This observation is consistent with the thrust kinematics in the Ertix shear zone in the Chinese Altai Mountains (Briggs et al., 2007).

The metamorphic complex directly above the Bulgan thrust, referred in this study as the Bodonch metamorphic belt (Fig. 1C and D), extends westward to the Chinese Altai Mountains region and correlates with the Ertix gneiss complex examined by Briggs et al. (2007). The Ertix gneiss complex, consisting of meta-pelite, meta-chert, and ~450 Ma orthogneiss experienced peak

pressure and temperature of 6.2–7.7 kbar and 560–670 °C at about 280 Ma (Briggs et al., 2007). Briggs et al. (2007) suggest that the gneiss complex is interpreted as an accretionary mélange under-thrust to a lower-crustal depth below an arc in the Carboniferous. The metamorphosed mélange complex together with the basal section of the arc was brought to the surface during post-ocean closure intra-continental thrusting along the Ertix fault and several north-dipping thrusts in its hanging wall from the Late Permian to the Jurassic (Briggs et al., 2007, 2009).

The Bodonch complex is mostly schist in the west and high-grade gneiss is east in our study area (Fig. 1C and D). In cross section view, the metamorphic grade is at a greenschist facies in the basal section, increasing to an amphibolite facies in the central section, and returning to a greenschist facies in the highest section (see schematic diagram in Fig. 1E). A similarly inverted metamorphic section in the hanging wall of the Ertix thrust zone in the Chinese Altai Mountains is also documented (Yang et al., 1992; Qu and Zhang, 1994), suggesting that this is a regional feature. Also note that inverted metamorphism is closely associated with the occurrence of leucogranites in the Cenozoic Himalayan orogen (Le Fort et al., 1987).

Foliation in the Bodonch metamorphic belt is generally east-striking and north-dipping, parallel to the foliation in the Bulgan thrust shear zone. Similar to the Ertix metamorphic complex in China, the metamorphic rocks in the Bulgan thrust hanging wall also consist of metapelite with the following mineral assemblage: mica + garnet + staurolite + cordierite + sillimanite + kyanite (Zorigtkhuu et al., 2011). This mineral assemblage is similar to that of meta-pelite in the high-grade Greater Himalayan Crystalline Complex (e.g., Le Fort et al., 1987) and similar to the meta-pelite assemblage in the Ertix gneiss complex (Briggs et al., 2007). High-grade schist and gneiss in the Bulgan belt are isoclinally folded, with amplitudes ranging from a few meters to a few kilometers (Polyanskii et al., 2011).

Biotite granite, biotite–muscovite granite, and garnet–muscovite and garnet–muscovite–tourmaline leucogranites occur widely in the hanging wall of the Bulgan thrust (Fig. 2A and B). The largest granitoid bodies are 10–40 km² in aerial extent (Fig. 1C), whereas the smallest intrusive bodies and leucosome veins that are 10s cm wide and a few m long cutting across gneissic foliation of the Bodonch complex (Fig. 2C). Most of the granitic bodies occur as sills with variable widths (a few meters to up to 80 m) emplaced parallel along gneissic foliation; as a result the granitic sills display a similar trend to the foliation and the Bulgan shear zone (Fig. 1C and D). In detail, the granitic and leucogranitic sills cross-cut one another, indicating they were emplaced at the about the same time. Most of the leucogranites are deformed, which are expressed by the development of gneissic foliation and formation of bundinage. Some sills are connected with irregularly shaped dikes that cut across foliation and early formed sills (Fig. 2B).

Biotite granite is common at the highest structural level whereas leucogranite is dominant in the lowest structural level. Mylonitized biotite granite (Fig. 2D) and garnet–tourmaline granite (Fig. 2E) in the Ertix shear zone display down-dip stretching lineation and top-south kinematic indicators in cross section. Undeformed granites and leucogranites are also present in the Bulgan thrust shear zone and have mutual cross-cutting relationships with the deformed leucogranites. The mutual cross-cutting relationships indicate that (1) strain is not homogeneously distributed across the Bulgan thrust-shear zone, (2) the Bulgan shear zone was not active all at once with different parts of the shear zones active at different times, and (3) the granites were emplaced during the development of the Bulgan shear zone. The mutual cross-cutting relationships among deformed and undeformed leucogranites in our study area are similar to those of the Himalayan leucogranites that were emplaced into the Greater Himalayan Crystalline Complex while it was deforming (Le Fort et al., 1987).

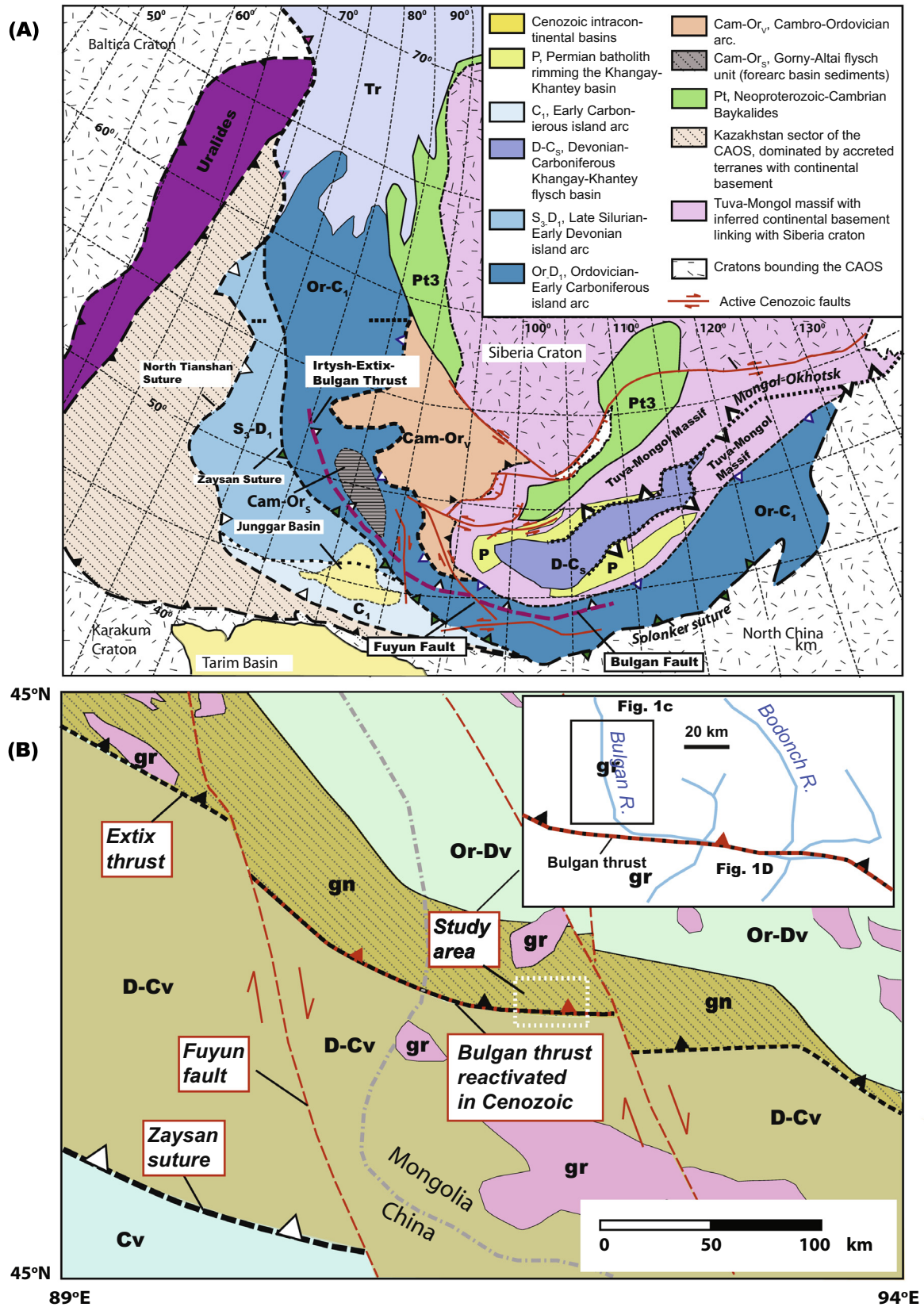


Fig. 1. (A) Simplified tectonic map of the Central Asian Orogenic System from Şengör and Natal'in (1996). Also shown are major Cenozoic faults taken mainly from Tapponnier and Molnar (1979) and Cunningham et al. (2003). (B) A geologic map compiled mainly from Ren (2002), Badarch et al. (2002), Briggs et al. (2007), and Stipska et al. (2010). Cenozoic faults are adopted mostly from Tapponnier and Molnar (1979), Cunningham et al. (1996, 1997, 2003) and Cunningham (1998, 2005). Inset map show the locations of the two geologic traverses conducted in this study. (C) Geologic map of the Bulgan River traverse. (D) Geologic map of the Bodonch River traverse and location of a schematic cross section line. (E) Schematic geologic cross section of the Bulgan thrust system and distribution of metamorphic grades.

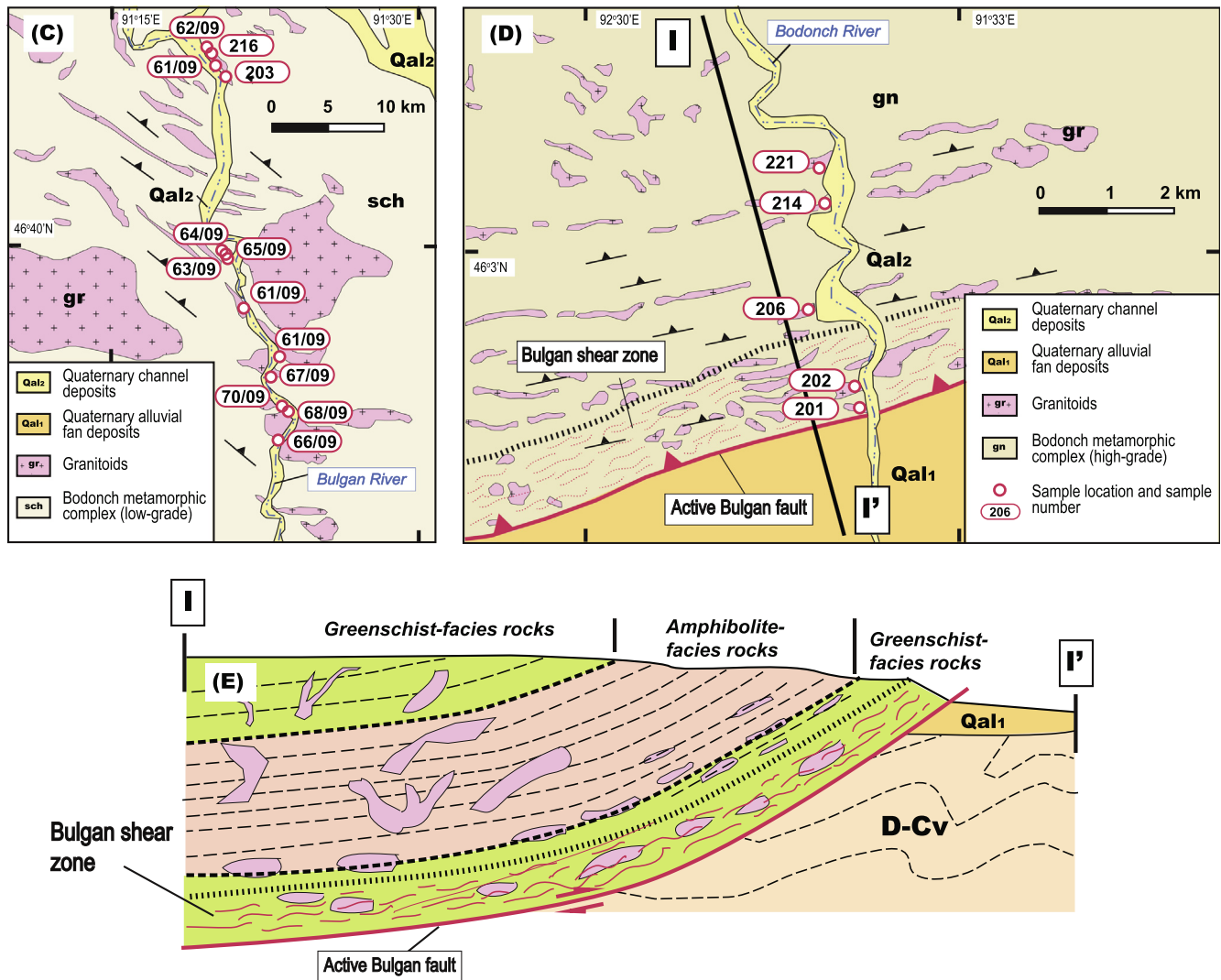


Fig. 1 (continued)

The occurrence of biotite granite at the highest structural level is also similar to the formation of the Tethyan Himalayan granitic belt that dominated by biotite granite (Harrison et al., 1998).

Marinov et al. (1973), who first described the granitoids exposed in the study area, assumed that the granites are interlayered with meta-sedimentary strata. In the geological maps of Yanshin (1978, 1989), only the biggest granitic bodies were shown. As a result, the granitic sills documented in this study were not investigated by the previous workers. A K–Ar cooling age of 152–153 Ma was obtained from one of the mapped granitic bodies (Marinov et al., 1973). Quartz–muscovite, quartz–beryllium–tourmaline with tungsten, and tantalum pegmatite are observed to intrude into the Bulgan metamorphic rocks. U–Pb SHRIMP zircon dating of the biotite–muscovite granite from this study yields a Late Triassic age of 215 ± 3.0 Ma (Fig. 3) (see more details below).

3. Petrography

3.1. Biotite–muscovite granite

We examined the petrography of the samples collected from the study area. Samples numbers and samples locations are shown in

Fig. 1C and D. Biotite–muscovite granite contains 45–50% microcline, 12–14% plagioclase, 28–30% quartz, and 12–15% combined biotite and muscovite. Accessory minerals include apatite, zircon, ilmenite and epidote. Largest crystals ($1.1 \times 1.65\text{--}1.45 \times 1.80$ mm) of microcline and plagioclases are zoned. Perthite and polysynthetic twinning strips are intersected, which are cut by younger fractures (Fig. 4A). Brittle fractures in quartz are filled by biotite, muscovite, sericite, and saussurite (Fig. 4B). Along sutured grain boundaries, the edges of K-feldspar and plagioclase were replaced by muscovite, epidote and saussurite. The biotite and muscovite, generally 1–3 mm long, are clustered and show preferred orientations that define lepidoblastic textures and stretching lineations. Recrystallized muscovite and biotite are also marked by sutured grain boundaries in biotite and muscovite. In some cases, micas are kinked and display mica fish in the S–C mylonitic rocks (Lister and Snoke, 1984). Myrmekite tends to occur along grain boundaries between plagioclase and K-feldspar. Apatite, ilmenite, zircon and epidote occur as inclusions in biotite and in groundmass that is cut by younger fractures and filled with saussurite aggregates. Biotite is altered to chlorite along cleavage planes. Ductile deformation is expressed by undulatory extinction of quartz with sutured boundaries and formation of subgrains and neoblasts around the rims of quartz and mica.

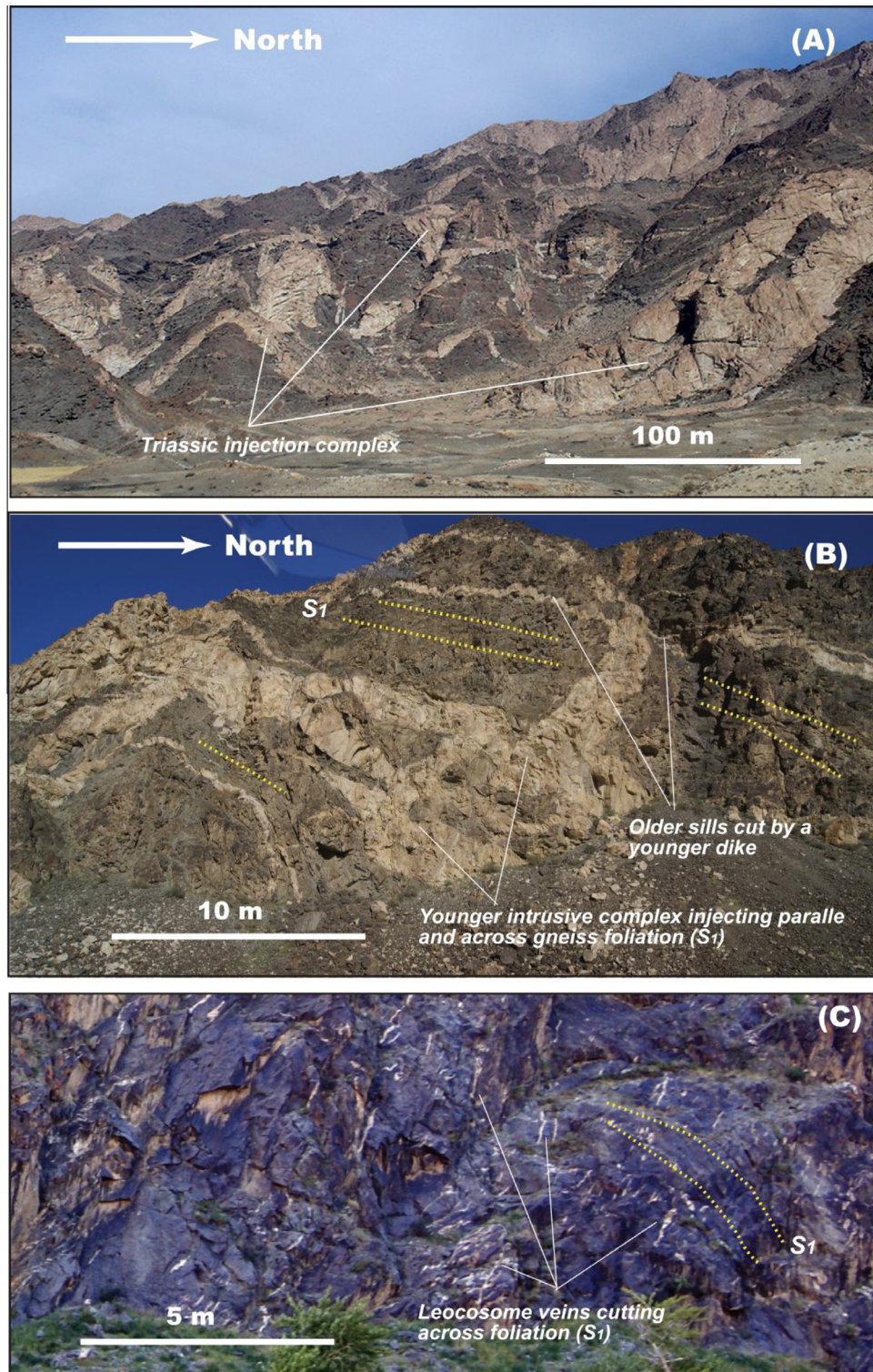


Fig. 2. (A) A granitic injection complex exposed in the hanging wall of the Bulgan thrust along the Bodonch River. (B) Sills and dikes in the Bodonch metamorphic complex exposed along the Bulgan River. Also shown are gneissic foliation and cross-cutting relationships among granitic intrusions. (C) Leucosomes intruded into the Bodonch metamorphic complex in the basal section of the Bodonch metamorphic complex along the Bulgan River. (D) Mylonitic biotite granite in the Bodonch metamorphic complex. (E) Mylonitic leucogranite in the Bodonch metamorphic complex.

3.2. Biotite granite

Biotite granite is comprised of 15–18% plagioclase, 28–30% quartz, 42–45% of K-feldspar, and 10–14% biotite. It typically exhibits porphyritic textures associated with euhedral plagioclase ($\sim 2.0 \times 1.4$ mm to 2.5×1.7 mm in size). Small biotite

(0.2–0.5 mm) grains are enclosed in plagioclase porphyry. Plagioclase is antiperthitic, whereas K-feldspar growth is stippled. Myrmecite is developed along K-feldspar–plagioclase contacts. Dark brownish (transmitted light) biotite displays sigmoidal shape due to ductile deformation. New grain boundaries and kink bands are all present in biotite (Fig. 4C). There are lozenge-shaped biotite aggregates that

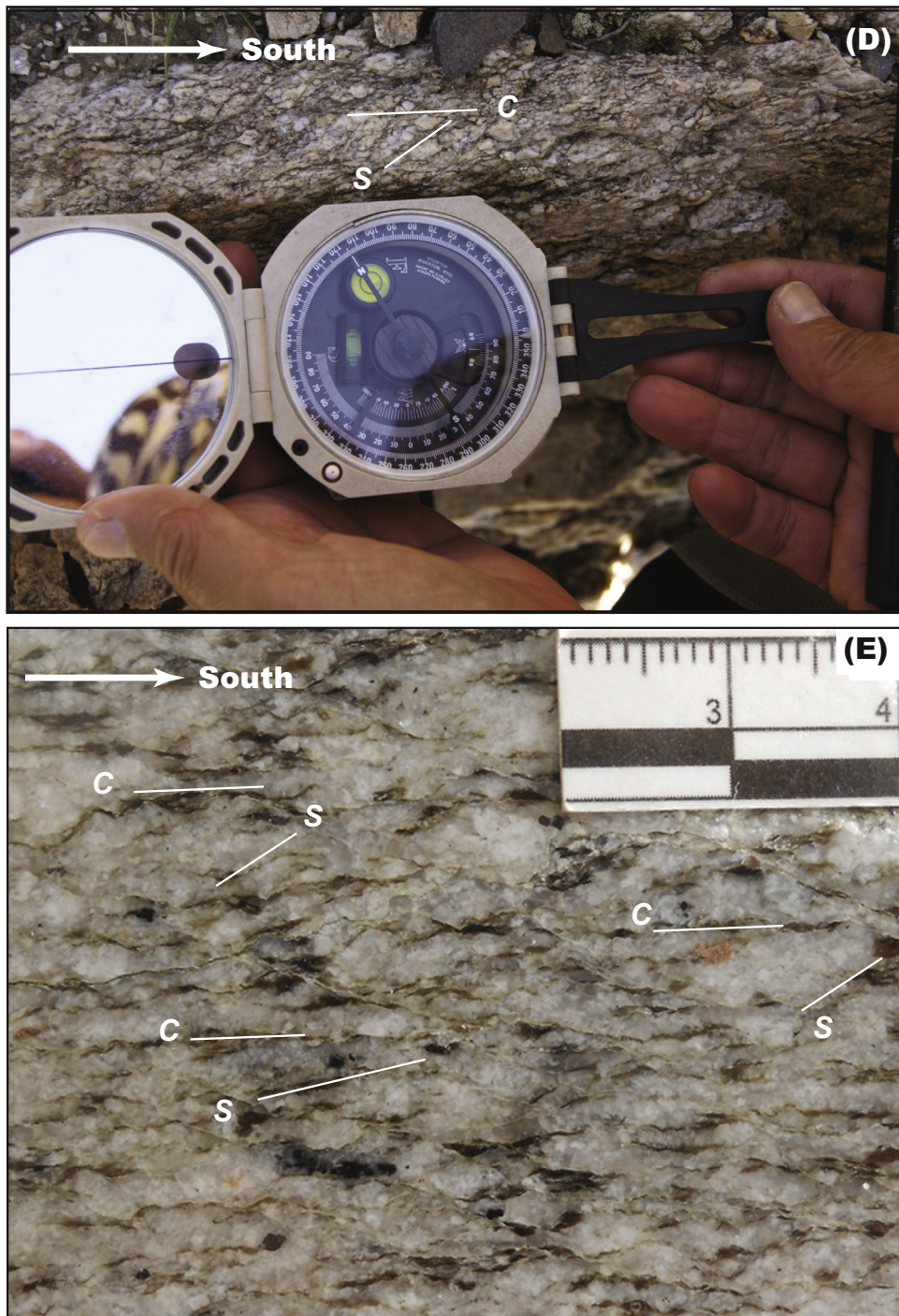


Fig. 2 (continued)

are akin to mica fish (Fig. 4D). New grains of epidote and saussurite were crystallized along sutured boundaries of feldspars (Fig. 4E and F). Subgrain boundaries in quartz or serrated edges of quartz are commonly accompanied by coronas of grains. Groundmass minerals are subhedral microcline perthite, plagioclase, quartz, and biotite. The microcline exhibits lattice twinning in interstice.

3.3. Leucogranites

Medium- to fine-grained leucogranites consist of tourmaline–muscovite, garnet–muscovite, and garnet–tourmaline–muscovite granites. Minerals in the leucogranites include 45–48% K-feldspar, 10–12% plagioclase, 28–30% quartz, 6–12% muscovite.

Garnet and tourmaline range in modal proportion from 1% to 5%. In some cases tourmalines occur in microclitic cavities. Plagioclase, microcline, and muscovite are porphyry-phase minerals, whereas microcline occurs mostly as phenocrysts. Plagioclase content is An_{10-12} . The primary igneous muscovite has a pale green color (transmitted light) (Fig. 4G). The groundmass consists of microcline, quartz, and oligoclase (Fig. 4H). The lattice microcline and muscovite are in the interstice. Accessory minerals in the leucogranites are fluorine and apatite. Tantalite and columbite were identified through heavy-mineral concentration.

Ductile deformation of the leucogranites is expressed by the formation of subgrains along sutured boundaries and undulatory extinction in quartz (Fig. 4I). Skeletal and fibrous muscovite occurs

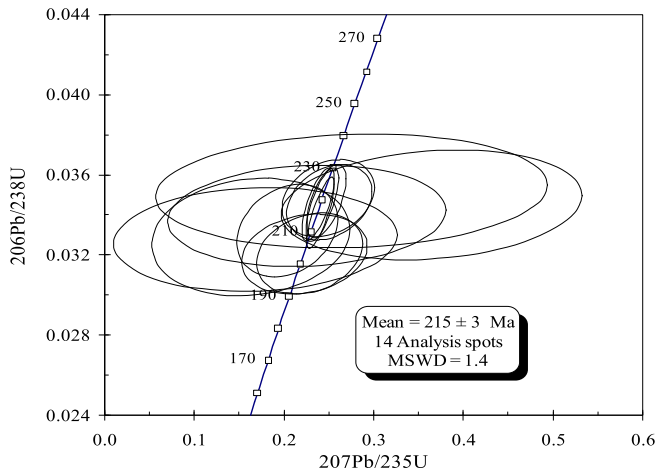


Fig. 3. U–Pb concordia diagram of zircon data obtained from a biotite–muscovite granite.

along the edges of muscovite (Fig. 4J) by replacement of K-feldspar and by recrystallization of primary igneous muscovite (Fig. 4K). The growth of sillimanite vibrolite was at the expense of primary igneous muscovite (Fig. 4L). From these textural relationships, we interpret that the garnet and epidote formed as porphyry minerals in an early phase of pluton crystallization. The aforementioned garnet is bright reddish color and has grain sizes from 0.5×0.5 to 3.0×3.0 mm. The garnet is fractured and filled by secondary muscovite. Secondary muscovite is altered from K-feldspar along garnet–epidote contacts. The birefringence color of the porphyry epidote is bluish yellow as a result of alteration to zoisite. The

groundmass consists of the same minerals as the porphyries, but microcline perthite is more common in the interstice of garnet–muscovite leucogranite.

4. Geochemistry and isotope dating of granitoids

4.1. Analytical procedures

Major elements were determined using X-ray fluorescence (XRF) spectroscopy at the Center for Instrumental Analyses at Yamaguchi University in Japan in 2009, and its analytical procedure is described in Yamasaki et al. (1999). The trace and rare earth elements were analyzed by inductively coupled plasma mass spectrometry (ICP-MS) at the Actlabs Co. Ltd., Canada. The obtained major, trace, and rare earth element contents are listed in Tables 1 and 2. The isotopic ratios were determined at the Actlabs Co. Ltd., Canada, with Sm and Nd separated by extraction chromatography on HDEHP covered Teflon powder. The isotopic analysis was performed on a Triton multi-collector mass spectrometer in the static mode. $^{143}\text{Nd}/^{144}\text{Nd}$ ratios are relative to the value of 0.511860 for the La Jolla standard. Rb and Sr were separated using conventional cation-exchange techniques. During the period of work the weighted average of 15 SRM-987 Sr-standard runs yielded ratios of 0.710256 ± 11 (2σ) for $^{87}\text{Sr}/^{86}\text{Sr}$. The $^{143}\text{Nd}/^{144}\text{Nd}$ and $^{87}\text{Sr}/^{86}\text{Sr}$ ratio data are shown in Table 3. Zircon dating was carried by analyzing U, Th and Pb contents using the sensitive high resolution ion microprobe (SHRIMP) at the Beijing SHRIMP Centre, administered by the Chinese Academy of Geological Sciences. The analytical procedure follows that of Compston et al. (1984), whereas the analytical data are shown in Table 4.

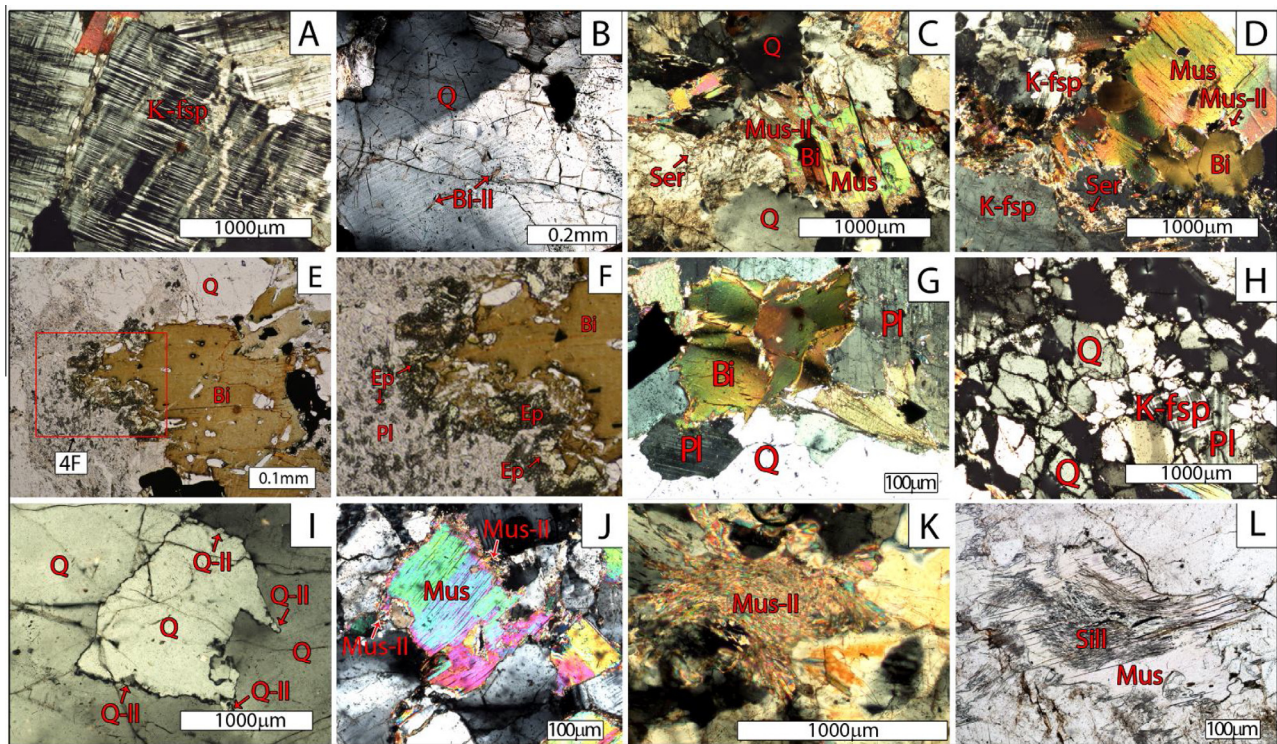


Fig. 4. Microscopic textures of deformed granites. (A) Plastic deformation of K-feldspar. (B) Plastically strained quartz and brittle fractures filled by mica. (C) Plastic and brittle deformation quartz expressed by undulation and fracture formation. Also shown is recrystallization of muscovite. (D) Sigmoidal porphyroblast and kink band in biotite and muscovite and the formation of saussurite aggregates by replacing K-feldspar along new grain boundaries. (E) Epidote and saussurites forming along suture boundaries of plagioclase and biotite. (F) Enlarged view from (E). (G) Biotite displaying mica-fish texture and sutures. (H) Cataclastic deformation in ground mass. (I) Sutures in quartz grains as a result of crystal-plastic deformations. (J) Muscovite recrystallization along crystal edges. (K) The secondary muscovite recrystallized along the boundaries of primary muscovite. (L) The sillimanite fibrolite formed at the expense of muscovite. Also see text for detailed description of each picture.

Table 1
Major element analyses from Triassic sheet-like granites in the western Mongolian Altai.

Sample no.	63/09 ^a (bi)	70/09 ^a (bi)	71/09 ^a (bi)	216 ^c (bi)	46.37.53	46.46.06	210 ^c (bi)	61/09 ^b (bi-ms)	62/09 ^c (bi-ms)	67/09 ^c (bi-ms)	214 ^b (bi-ms)	221 ^b (bi-ms)	64/09 ^a (gar-ms)	68/09 ^a (gar-ms)	69/09 ^d (gar-ms)	206 ^b (gar-ms)	65/09 ^a (tour-ms-)	66/09 ^a (tour-ms-)	72/09 ^a (gar-tour-ms)	203 ^a (gar-tour-ms)	201 ^b (apl)	202 ^b (apl)
Position	46.39.48	46.34.24	46.37.53	46.46.06	46.36.14	46.36.12	46.36.14	46.46.30	46.46.43	46.35.35	46.3.15	46.3.27	46.39.41	46.34.37	46.14.15	46.2.40	46.39.23	46.33.30	46.31.6	46.45.41	46.2.7	46.2.15
wt%	91.20.30	91.23.33	91.21.26	91.20.02	91.23.12	91.23.12	91.23.12	91.19.49	91.19.37	91.22.50	92.31.55	92.31.52	91.20.40	91.23.24	91.23.36	92.31.47	91.20.39	91.23.8	91.23.19	91.20.39	92.32.13	92.32.10
SiO ₂	66.44	67.32	68.49	69.0	71.49	70.47	70.47	70.47	73.98	73.97	74.22	73.2	73.96	73.27	75.31	71.28	73.24	74.82	73.65	74.47	75.61	74.48
TiO ₂	0.78	0.81	0.63	0.47	0.36	0.39	0.36	0.39	0.27	0.21	0.26	0.74	0.03	0.02	0.04	0.84	0.01	0.08	0.08	0.3	0.07	0.08
Al ₂ O ₃	15.51	14.81	14.86	15.8	15.67	15.03	14.24	15.03	13.32	13.94	14.24	14.11	14.45	14.77	14.86	15.08	14.85	14.44	13.88	14.43	14.16	14.64
Fe ₂ O ₃	4.43	4.4	3.77	2.8	2.04	2.8	2.04	2.8	1.92	1.90	1.10	1.72	1.14	0.85	1.02	2.29	0.85	1.09	0.82	1.01	1.05	1.09
MnO	0.08	0.08	0.07	0.04	0.06	0.06	0.06	0.06	0.04	0.04	0.01	0.04	0.02	0.12	0.15	0.19	0.03	0.03	0.01	0.05	0.03	0.01
MgO	1.16	1.24	1.01	1.4	0.06	0.54	0.41	0.29	0.41	0.29	0.41	0.51	0.17	0.04	0.07	0.54	0.05	0.15	0.09	0.02	0.16	0.21
CaO	2.41	2.59	2.24	1.53	1.6	1.53	1.6	1.53	1.23	0.62	0.63	1.12	1.22	0.27	0.35	2.64	0.28	0.53	0.57	0.43	1.10	0.53
Na ₂ O	3.22	3.2	3.14	3.03	3.21	3.48	3.21	3.48	2.8	3.29	2.62	3.74	3.58	3.22	4.18	3.25	3.19	3.55	2.93	4.08	3.40	3.33
K ₂ O	4.69	4.31	4.72	5.04	4.94	4.71	4.94	4.71	5.0	4.68	6.17	4.23	4.37	6.5	3.37	3.62	6.54	4.67	6.82	4.29	4.07	5.02
P ₂ O ₅	0.18	0.19	0.15	0.21	0.18	0.12	0.18	0.12	0.08	0.11	0.21	0.09	0.08	0.11	0.09	0.12	0.11	0.06	0.05	0.12	0.13	0.11
Total	98.9	98.95	99.08	99.32	99.59	99.13	99.59	99.13	99.05	99.05	99.87	99.5	99.02	99.17	99.44	99.85	99.24	99.42	98.9	99.2	99.78	99.5
A/(C+N+K)	1.20	1.15	1.05	1.15	1.14	1.11	1.14	1.11	1.09	1.13	1.03	1.16	1.05	1.16	1.22	1.02	1.01	1.04	1.33	1.32	1.21	1.22
Al ₂ O ₃ /TiO ₂	19.88	18.28	23.59	33.62	43.53	38.54	43.53	38.54	49.33	66.38	54.77	19.07	481.67	738.50	371.50	17.95	1485.0	180.50	173.5	48.10	202.29	183.00
CaO/Na ₂ O	0.75	0.81	0.71	0.50	0.50	0.44	0.50	0.44	0.44	0.19	0.24	0.30	0.34	0.08	0.08	0.81	0.09	0.15	0.19	0.11	0.32	0.16

Notes: Fe₂O₃, measured as total iron content; (bi) – biotite granite and granodiorite; (bi-ms) – biotite-muscovite granite; (gar-ms) – garnet-muscovite granite; (tour-ms) – tourmaline-muscovite granite; (gar-tour-ms) – garnet-tourmaline-muscovite leucogranite; apl – aplite.

^a Samples from Bulgan area.

^b Samples of Bodonch area.

^c Sample analyzed for age and isotope.

^d Sample used only for isotope data.

4.2. Geochemistry

We analyze major and trace elements of the collected plutonic samples and their results are shown in Table 1. Also listed in Table 1 are sample numbers with their corresponding locations shown in Fig. 1C and D. In the R1–R2 classification scheme (De la Roche et al., 1980), where $R1 = 4Si - II(Na + K) - 2(Fe + Ti)$ and $R2 = A1 + 2Mg + 6Ca$, our samples are plotted in granite, granodiorite, and alkali granite fields (Fig. 5A). Specifically, the garnet-muscovite granite (with silica content 71.28%) and biotite granite samples are plotted in the granodiorite field, the garnet-tourmaline and muscovite granite samples are plotted in the alkali granite, and the garnet muscovite granite samples are plotted in the alkali granite field (Fig. 5A). For comparison, we also plot the two mica leucogranite samples of Guo and Wilson (2012) from the Himalaya on the same diagram (Fig. 5A), which indicates that our data overlap in general the data from the Himalaya. Noticeably, our samples are plotted in a wider field extending to the higher R1 values in the field of granodiorite and to the lower R1 values in the field of alkali granite (Fig. 5A). In the A/NK-A/CNK classification scheme of Maniar and Piccoli (1989) (Fig. 5B), all of our samples are plotted in the peraluminous field, which is indicated by the A/CNK ratio >1.1. The highest A/CNK ratios, ranging from 1.12 to 1.33, are found in aplite and muscovite granite samples (Fig. 5B).

As shown in Table 1, the granites have relatively low content of CaO with higher than average K₂O/Na₂O ratios. The iron oxide, measured as total iron, ranges from 3.37% to 4.43% for the biotite granite sample, from 1.90% to 2.80% for the biotite-muscovite granite, and 0.82% to 1.14% for the muscovite, garnet-muscovite, and garnet-tourmaline-muscovite leucogranites. The high Al₂O₃/TiO₂ ratio of 173.5–1485 measured from leucogranites exceed that found in the biotite granite (18.28–23.58) and the biotite-muscovite granite (38.5–66.8). The high Al₂O₃/TiO₂ ratios indicate that the protolith of the leucogranites were pelitic and psammitic rocks (Sylvester, 1998).

The CaO/Na₂O ratio is 0.71–0.80 for the biotite granite samples and 0.07–0.43 for the aplite, muscovite, garnet-muscovite, garnet-tourmaline-muscovite leucogranite samples with only one exception as high as 1.21. The higher CaO/Na₂O ratios suggest higher melting temperatures of the source rocks for the biotite granite. The Rb/Sr ratio is low (0.51–1.82) for the biotite, biotite-muscovite, and aplite granite samples, and high (>6.7) for the garnet-muscovite and garnet-tourmaline-muscovite leucogranite samples. Rb/Sr ratios similar to those for the biotite, biotite-muscovite, and aplite granite samples have been observed from the Himalayan biotite, and garnet-muscovite granites, which are indicative of vapor-absent melting conditions (Harris et al., 1993, 1995) and are consistent with a higher melting temperature for the this suite of rocks than that for leucogranites as inferred from the CaO/Na₂O ratio.

We use the Harker diagrams to plot oxides against SiO₂ measured from our samples (Fig. 6A–D). The biotite granite sample yields higher Al₂O₃ contents (14.7–15.8%) and lower SiO₂ contents (66–71.5%) than those obtained from the biotite-muscovite granite, aplite, and leucogranite samples (Fig. 6A). In the CaO vs. SiO₂ plot (Fig. 6B), the biotite granite samples have higher CaO values and lower SiO₂ values than those measured from the biotite-muscovite granite and leucogranite samples. In the Na₂O vs. SiO₂ plot, the biotite granite and aplite samples yield a narrow range of Na₂O values, at 2.9–3.2% for the biotite granite sample and at 3.3–3.4% for the aplite sample. In contrast, the biotite-muscovite granite and leucogranite samples show a large range of variation in the Na₂O values, at 2.5–3.9% for the biotite-muscovite granite samples and at 2.8–4.2% for the leucogranite samples (Fig. 6C). In the K₂O vs. SiO₂ plot, all our samples are plotted in the high-K field except

Table 2
Trace and REE element analyses from Triassic sheet-like granites in the western Mongolian Altai.

Sample no.	63/09 ^a (bi)	70/09 ^a (bi)	71/09 ^a (bi)	216 ^a (bi)	210 ^a (bi)	61/09 ^a (bi–ms)	62/09 ^c (bi–ms)	67/09 ^a (bi–ms)	214 ^b (bi–ms)	221 ^b (bi–ms)	64/09 ^a (gar–ms)	68/09 ^a (gar–ms)	69/09 ^d (gar–ms)	206 ^b (gar–ms)	65/09 ^a (tour–ms–)	66/09 ^a (tour–ms–)	72/09 ^a (gar–tour–ms)	203 ^a (gar–tour–ms)	201 ^b (apl)	202 ^b (apl)
Li (0.5)	30.4	38.8	32.6	0.50	0.50	76.3	45.4	113	0.24	0.30	26.8	9.4	18.0	0.81	22.6	14.7	8.1	0.11	0.32	0.16
Be (0.1)	3.8	3.5	4.1	2.5	2.8	9.5	6.5	10.8	1.0	3.8	7.5	90.6	229	4.2	10.2	12.7	6.0	8.1	1.6	1.8
Cs (0.05)	5.31	3.87	5.66	7.74	6.34	12.8	8.87	6.8	4.36	5.94	15.1	8.09	1.88	1.75	14.8	12.4	11.7	41.2	3.64	2.13
Th (0.1)	7.3	6.9	12.6	11.5	29.5	19.0	5.8	11.6	19.4	7.9	2.0	0.7	0.7	0.95	3.1	2.5	5.1	5.8	13.0	14.9
U (0.1)	1.9	1.8	1.2	0.9	1.5	1.4	2.8	4.3	0.9	0.9	1.7	2.2	1.1	3.1	2.2	2.1	1.5	1.4	1.3	2.7
Pb (0.05)	25.1	19.6	24.3	28.2	36.3	28.5	22.3	19.0	57.9	19.9	59.6	18.2	12.2	22.4	46.0	23.5	47.9	16	20.4	22
Ga (0.1)	22.5	19.3	19.2	17.9	21	22.9	17.8	24.2	7.6	19.1	14.5	23.4	22	12.1	26.2	29.7	23.3	28.8	13.4	12.4
Rb (0.2)	95.7	84.9	133	170	137	236	195	359	136	122	159	291	225	288.4	233	271	229	398	145	144
Sr (0.2)	174	166	196	136	102	130	136	44.5	209	70.7	60.2	10.5	2.9	3.19	14	36.7	34.2	33.2	222	154
Ba (1)	543	482	569	485	880	446	389	132	770	300	226	23	9	13.1	60	73	103	78	471	333
Zr (1)	13	17	11	22	30	45	2	20	14	67	7	3	3	5.1	5	2	6	20	83	60
Hf (0.1)	0.7	0.8	0.4	0.8	1.0	1.4	0.1	0.5	0.5	2.3	0.2	0.2	0.1	0.4	0.2	0.1	0.1	0.6	2.8	2.4
Ta (0.1)	0.8	2.6	0.1	0.2	0.1	1.1	0.1	0.6	0.9	1.1	0.4	1.9	1.2	1	0.2	0.1	0.1	2.5	1.1	1.4
Nb (0.1)	29	36.6	1	4.8	1.1	12.6	3.8	8.1	4	17.8	2.7	11.9	8.5	9.6	5.3	4.8	6.8	11.6	8.9	9
La (0.1)	32.8	17.7	39.5	25.9	68.7	54.7	21.6	24.6	28.4	19.1	6.9	1.2	1.8	3.2	5.6	5.5	12.1	6.2	12.4	12
Ce (0.1)	68.2	53.4	78.4	58.2	149	116	37.5	50.5	60.1	55.5	13.5	1.8	2.6	3.8	12.7	11.3	22.3	13.9	29.8	22.2
Pr (0.1)	6.6	5.1	9.1	6.8	17	14.1	4.4	6.3	6.7	4.7	1.9	0.2	0.3	0.4	1.7	1.5	3.2	1.6	2.4	2.1
Nd (0.1)	20.5	17.5	28.9	26.2	60.9	40.5	11.6	17.3	23.9	17.6	6.2	0.6	0.8	0.9	6.8	4.2	8.8	5.8	7.8	7.1
Sm (0.1)	4.6	4.1	5.6	5.6	12.3	6.9	2.0	3.1	5.1	3.8	1.6	0.1	0.2	0.4	1.5	1.0	1.9	1.3	1.6	1.5
Eu (0.05)	1.37	1.18	1.72	1.07	1.5	1.23	0.95	0.35	0.92	0.55	0.37	0.05	0.05	0.18	0.32	0.21	0.44	0.17	0.34	0.32
Ho (0.1)	0.8	0.8	0.9	0.8	1.7	0.8	0.5	0.4	0.8	0.9	0.4	0.1	0.1	0.2	0.3	0.3	0.3	0.3	0.3	0.3
Er (0.1)	2	2.2	2.2	1.9	4.3	2.3	1.5	1.2	2.2	2.5	1	0.2	0.3	0.5	0.7	0.9	1	0.8	0.9	0.9
Gd (0.1)	5.6	5.3	6.5	5.3	11.3	6.6	2.3	2.5	4.9	4.2	2.1	0.2	0.2	0.6	1.9	0.9	1.5	1.3	1.5	1.5
Tb (0.1)	0.8	0.7	0.8	0.8	1.6	0.8	0.4	0.4	0.7	0.7	0.4	0.1	0.1	0.2	0.3	0.2	0.2	0.2	0.2	0.3
Dy (0.1)	3.5	3.8	4.1	4.3	9	3.8	2.2	1.9	4	4.3	1.9	0.2	0.3	1.1	1.6	1.0	1.3	1.4	1.4	1.5
Tm (0.1)	0.3	0.3	0.3	0.2	0.6	0.4	0.2	0.2	0.3	0.3	0.2	0.1	0.1	0.2	0.2	0.2	0.2	0.1	0.1	0.1
Yb (0.1)	1.8	1.9	1.7	1.4	3.3	1.9	1.2	1.0	1.6	2.1	0.9	0.3	0.5	0.3	1.4	1.2	1.1	0.9	1.0	1.1
Lu (0.1)	0.3	0.3	0.3	0.2	0.4	0.3	0.1	0.1	0.2	0.3	0.1	0.1	0.1	0.1	0.2	0.2	0.2	0.1	0.2	0.2
Y (0.1)	18.5	16.3	17.7	19.4	42.9	19.4	11.2	10.6	19.8	21.0	9.4	1.7	1.7	2.8	5.0	7.8	9.1	8.9	9.2	9.4

Table 3
Nd and Sr isotope ratios.

Sample number	$^{87}\text{Sr}/^{86}\text{Sr}$	Uncertainly (2 sigma)	$^{143}\text{Nd}/^{144}\text{Nd}$	Uncertainly (2 sigma)
62	0.718558	6	0.512553	3
69*	1.309609	12	0.512559	13
69*	1.323161	7		

Note: Sm and Nd were separated by extraction chromatography on HDEHP covered Teflon powder. The analysis was performed on Triton multi-collector mass-spectrometer in static mode. $^{143}\text{Nd}/^{144}\text{Nd}$ ratios are relative to the value of 0.511860 for the La Jolla standard. Rb and Sr were separated using conventional cation-exchange techniques. The analysis was performed on Triton multi-collector mass-spectrometer in static mode. During the period of work the weighted average of 15 SRM-987 Sr-standard runs yielded 0.710256 ± 11 (2 s) for $^{87}\text{Sr}/^{86}\text{Sr}$. Sample 69* is heterogeneous and it was homogenized before decomposition for second analysis.

two data points from the biotite granite samples (Fig. 6D) (Rickwood, 1989).

The geochemical characteristics of our samples can be further distinguished by their trace element contents. In the U vs. Th plot, data points from the leucogranite samples can be separated from those from the biotite granite, biotite–muscovite granite, and aplite samples by their low Th contents (<7 ppm) and a moderate range of variation in the U content (1.1–3.2 ppm) (Fig. 6E). Data points of the biotite granite and aplite samples are clustered in their own respective fields and can be separated from one another and from the data points of the aforementioned leucogranite samples in the U vs. Th plot (Fig. 6E). In contrast to their distinctive ranges of U and Th values, data points from the biotite–muscovite granite samples spread over a wide range of U and Th contents, which overlap the data points obtained from the leucogranite and aplite samples (Fig. 6E). In the Ta vs. Nb plot, all samples display a trend of increasing Ta with increasing Nb (Fig. 6F). In particular, the leucogranite samples have the steepest slope, whereas the biotite granite samples have the largest range of Nb values. In the Zr vs. Hf plot, all samples show a positive linear correlation between Zr and Hf with a similar slope (Fig. 6G).

In the Fig. 6H except studied granites we plot Rb/Ba vs. Rb/Sr data of schists and metapelite of our study and of Jiang et al. (2012). The granites show same distribution of Himalayan and Alps peraluminous granites (Sylvester, 1998). The plot shows that the biotite granite, two mica granite, and metapelite samples are plotted in the clay-poor sources, whereas the leucogranite samples from this study are plotted in the field clay rich sources. The inferred clay-rich sources for the occurrences garnet leucogranites in the study area from Fig. 6H are consistent with the presence of calcite, epidote and hornblende in the Devonian–Carboniferous metasediment–volcanic strata in the footwall of the Bulgan thrust shear zone. Carbonate rocks may have also been involved in the anatexis creating the observed leucogranites, which is indicated by the CO_2 dominant fluid inclusions in quartz in the pelitic schist along the Bulgan thrust shear zone in the Bodonch area (Zorigtkhuu et al., 2012).

In the primitive-mantle-normalized multi-element diagram (Sun and McDonough, 1989), the trace element patterns show positive anomalies for Cs, Rb, Th, U, and Pb, and negative anomalies for Nb and Sr (Fig. 7A). Garnet–muscovite, tourmaline–muscovite, and garnet–tourmaline–muscovite leucogranite samples display more pronounced negative anomalies of Ba and Sr than other granite samples. The trace-element trends of the leucogranite samples for Ba, Th, Pb, Nb and Sr are similar to those of pelagic and terrigenous sediments of an oceanic trench as source rocks of forearc granites in southwest Japan (Shimoda et al., 2003). The La, Ce, Nd, Zr and Hf distributions are variable for the granite samples (Fig. 7A). A sedimentary component in the magma source of the granite samples is suggested by the high concentrations of P_2O_5 , Li, Be, U, and Th (Plank and Langmuir, 1998). The lithium content ranges from 45 to 113 ppm as detected from biotite–muscovite

granite, whereas a high concentration of beryllium (90.6–229 ppm) was obtained from the garnet–muscovite granite (Table 1).

In the mantle-normalized rare earth element (REE) diagram (Fig. 7B), muscovite and garnet–muscovite leucogranite samples are characterized by stronger REE depletion compared to those of the biotite, and biotite–muscovite granite samples. In comparison, the REE pattern is intermediate for the aplite sample between the leucogranite and granite samples. The La/Yb ratio is 4.58–11 for the leucogranite samples and 9.32–28.79 for the biotite and biotite–muscovite granite samples (Table 1). Slightly negative Eu anomalies characterize most rock samples, although the biotite–muscovite and some leucogranite samples display positive Eu anomalies (Fig. 7B). A negative Eu anomaly and high Rb/Sr ratios indicate either feldspar fractionation or residual feldspar in the source rock (Inger and Harris, 1993).

4.3. Isotope analysis

The $^{87}\text{Sr}/^{86}\text{Sr}$ ratio is 0.7185 and the $^{143}\text{Nd}/^{144}\text{Nd}$ ratio is 0.512553 for a biotite–muscovite granite sample (Table 3). The initial isotopic ratios (Sr_i and Nd_i) are 0.7058 and 0.5124, respectively, for the same two-mica granite sample. For the garnet–muscovite leucogranite, the $^{87}\text{Sr}/^{86}\text{Sr}$ ratio ranges from 1.3096 to 1.3231 and the $^{143}\text{Nd}/^{144}\text{Nd}$ ratio is 0.512559. The Sr_i is 0.582819 for the same garnet–muscovite granite sample has Sr content of 2.9 ppm and Rb content of 225 ppm. The Nd_i of the garnet–muscovite granite sample is 0.5123. The $^{87}\text{Sr}/^{86}\text{Sr}$ and $^{143}\text{Nd}/^{144}\text{Nd}$ ratios indicate that the garnet–muscovite granite was derived from melting of terrigenous sediments (Basu et al., 1990) and/or highly differentiated upper crustal rocks (Davies et al., 1983). Specifically, the $^{87}\text{Sr}/^{86}\text{Sr}$ isotope ratios and ϵNd (–0.29) suggest that the garnet–muscovite granite was derived from melting of pelitic and psammitic rocks (Basu et al., 1990).

4.4. U–Pb zircon dating

Fourteen SHRIMP spots were analyzed in fourteen zircon grains collected from a biotite–muscovite granite sample. The U–Pb isotopic data are plotted in a concordia diagram (Fig. 3) and the corresponding analytical data can be found in Table 4. The obtained ages range from 203 to 220 Ma, with an weighted mean age at 215 ± 2.9 Ma. Although micro fissure and residual solutions are present, we did not detect xenocore and recrystallized rims from dated zircon grains. Back-scatter detector (BSD) and Cathodoluminescence (CL) imaging of dated zircon grains indicates that all zircon is euhedrally zoned near the rims (Fig. 8), which can be interpreted as a result of homogenous melting during crystallization of the granite. Based on the above textural argument, we suggest that the emplacement of the dated biotite–muscovite granite occurred at 215 ± 2.9 Ma.

Table 4
U–Pb data for zircon dating

Spot	²⁰⁶ Pbc %	ppm U	ppm Th	²³² Th/ ²³⁸ U	ppm ²⁰⁶ Pb*	(1) ²⁰⁶ Pb/ ²³⁸ U age	(2) ²⁰⁶ Pb/ ²³⁸ U age	(3) ²⁰⁶ Pb/ ²³⁸ U age	(1) ²⁰⁷ Pb/ ²⁰⁶ Pb age	(1) ²⁰⁸ Pb/ ²³² Th age	% Discordant	Total ²³⁸ U/ ²⁰⁶ Pb	±%						
1.1	0.33	1139	163	0.15	33.9	218.9 ± 4.6	219.0 ± 4.7	219.1 ± 4.7	195 ± 51	208 ± 11	–12	28.87	2.1						
2.1	1.08	405	57	0.14	12.2	220.9 ± 4.9	220.3 ± 4.9	220.6 ± 5.0	283 ± 190	232 ± 46	22	28.40	2.2						
3.1	0.96	420	81	0.20	12.6	219.6 ± 4.8	218.9 ± 4.8	219.5 ± 5.0	307 ± 170	221 ± 26	29	28.60	2.2						
4.1	0.48	1034	120	0.12	31.0	219.9 ± 4.7	219.5 ± 4.7	220.2 ± 4.8	272 ± 66	200 ± 22	19	28.69	2.1						
5.1	3.09	440	139	0.33	12.5	204.0 ± 5.2	203.2 ± 5.1	204.5 ± 5.5	272 ± 230	189 ± 27	25	30.21	2.5						
6.1	1.79	174	53	0.31	5.07	210.9 ± 5.9	212.1 ± 5.9	211.6 ± 6.2	–83 ± 270	193 ± 26	355	29.58	2.8						
7.1	4.29	63	115	1.89	1.95	219.4 ± 7.0	211.5 ± 6.8	215 ± 10	1.113 ± 370	228 ± 13	80	27.75	3.0						
8.1	2.36	137	114	0.86	3.86	203.7 ± 5.1	203.3 ± 4.9	204.9 ± 5.9	215 ± 290	194 ± 13	5	30.47	2.4						
9.1	5.42	96	139	1.49	2.96	216.2 ± 6.4	215.9 ± 5.7	216.2 ± 8.3	113 ± 650	214 ± 17	–92	27.85	2.6						
10.1	5.59	61	93	1.57	1.96	224.0 ± 7.2	221.3 ± 7.0	225 ± 11	486 ± 710	218 ± 26	54	26.83	2.8						
11.1	3.68	159	95	0.62	4.66	209.2 ± 7.5	212.3 ± 7.5	212.2 ± 8.5	–624 ± 750	177 ± 26	134	29.3	3.5						
12.1	5.94	82	120	1.51	2.45	208.9 ± 6.6	211.2 ± 5.9	216.5 ± 8.6	–530 ± 1000	181 ± 18	140	28.70	2.8						
14.1	0.05	1125	272	0.25	33.0	216.1 ± 4.5	215.9 ± 4.6	216.3 ± 4.7	249 ± 35	211.5 ± 5.8	13	29.32	2.1						
14.1	0.20	744	129	0.18	22.1	218.7 ± 4.7	218.6 ± 4.7	218.7 ± 4.8	241 ± 49	220 ± 11	9	28.92	2.2						
Total ²⁰⁷ Pb/ ²⁰⁶ Pb	±%	(1) ²³⁸ U/ ²⁰⁶ Pb*	±%	(1) ²⁰⁷ Pb*/ ²⁰⁶ Pb*	±%	(1) ²⁰⁷ Pb*/ ²³⁵ U	±%	(1) ²⁰⁶ Pb*/ ²³⁸ U	±%	Err. corr.	(3) ²³⁸ U/ ²⁰⁶ Pb*	±%	(3) ²⁰⁷ Pb*/ ²⁰⁶ Pb*	±%	(3) ²⁰⁷ Pb*/ ²³⁵ U	±%	(3) ²⁰⁶ Pb*/ ²³⁵ U	±%	Err. corr.
0.05265	1.5	28.96	2.1	0.0500	2.2	0.2381	3.1	0.03454	2.1	.701	28.92	2.1	0.05095	1.5	0.2429	2.6	0.03457	2.1	.819
0.0606	4.4	28.71	2.3	0.0519	8.1	0.250	8.4	0.03486	2.3	.268	28.72	2.2	0.0510	5.2	0.245	5.7	0.3482	2.2	.391
0.0601	5.3	28.88	2.2	0.0519	7.4	0.251	7.7	0.03465	2.2	.286	28.86	2.2	0.0523	6.2	0.250	6.6	0.3465	2.2	.336
0.05554	1.6	28.83	2.2	0.0517	2.9	0.2474	3.6	0.03470	2.2	.598	28.77	2.1	0.05307	1.7	0.2543	2.8	0.3476	2.1	.781
0.0763	2.4	31.18	2.6	0.0516	10	0.229	11	0.03215	2.6	.243	30.99	2.5	0.0548	3.5	0.244	4.3	0.03227	2.5	.584
0.0589	3.5	30.12	2.8	0.0445	11	0.204	11	0.03325	2.8	.253	29.95	2.8	0.0480	4.3	0.221	5.2	0.03339	2.8	.540
0.1098	9.0	28.99	3.2	0.077	19	0.366	19	0.0346	3.2	.171	29.34	3.0	0.064	16	0.299	17	0.0341	3.0	.179
0.0692	3.4	31.21	2.5	0.0504	13	0.223	13	0.03210	2.5	.197	30.95	2.4	0.0561	4.2	0.250	4.9	0.03232	2.4	.499
0.0916	5.2	29.45	3.0	0.048	28	0.227	28	0.0341	3.0	.107	29.25	2.6	0.0504	10	0.237	10	0.03419	2.6	.253
0.101	11	28.42	3.3	0.057	32	0.227	32	0.0354	3.2	.100	28.06	2.8	0.064	19	0.313	19	0.03564	2.8	.148
0.0659	8.1	30.4	3.6	0.0360	27	0.164	28	0.0330	3.6	.132	29.9	3.5	0.0493	11	0.228	12	0.0335	3.5	.301
0.0855	5.1	30.52	3.2	0.037	38	0.170	38	0.0329	3.2	.083	29.25	2.8	0.0695	6.4	0.328	6.9	0.03418	2.8	.398
0.05161	1.5	29.33	2.1	0.0511	1.5	0.2406	2.6	0.03409	2.1	.813	29.31	2.1	0.05189	1.5	0.2441	2.6	0.03412	2.1	.822
0.05263	1.7	28.98	2.2	0.0510	2.1	0.2427	3.1	0.03451	2.2	.714	28.98	2.2	0.05089	1.8	0.2421	2.8	0.03451	2.2	.778

Note: Errors are 1-sigma; Pbc and Pb* indicate the common and radiogenic portions, respectively. Error in standard calibration was 0.53% (not included in above errors but required when comparing data from different mounts). (1) Common Pb corrected using measured ²⁰⁴Pb. (2) Common Pb corrected by assuming ²⁰⁶Pb/²³⁸U–²⁰⁷Pb/²³⁵U age-concordance. (3) Common Pb corrected by assuming ²⁰⁶Pb/²³⁸U–²⁰⁸Pb/²³²Th age-concordance.

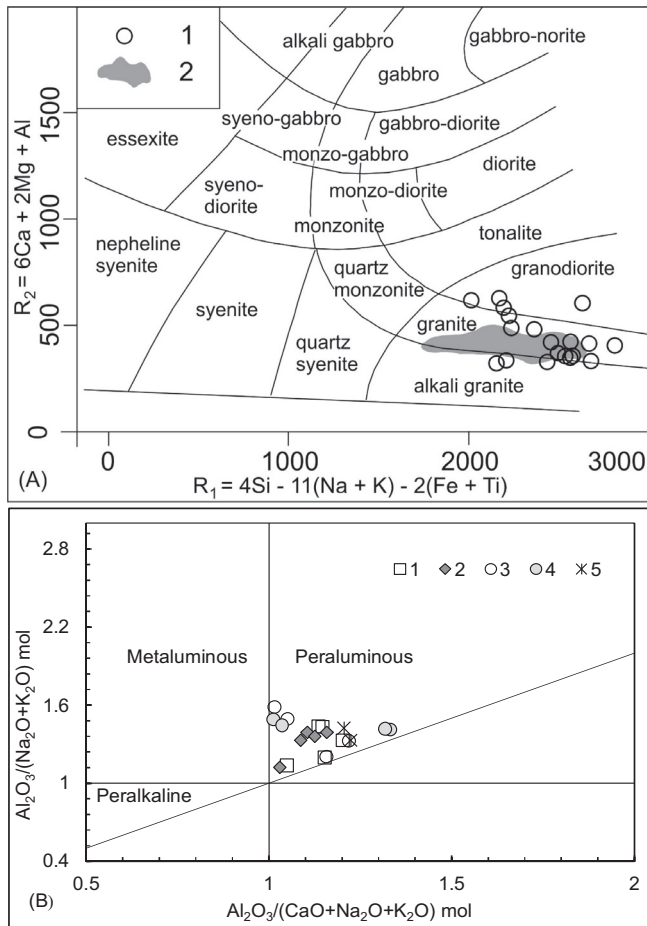


Fig. 5. (A) Classification of granitoid samples using the R1–R2 scheme of De la Roche et al. (1980). 1 = data from granite samples of this study; 2 = data from garnet and two-mica Himalayan leucogranites of Guo and Wilson (2012). (B) Composition of the granites examined in this study in the A/NK–A/CNK plot of Maniar and Piccoli (1989). 1 = biotite granite, 2 = biotite–muscovite granite, 3 = garnet–muscovite granite, 4 = tourmaline–muscovite and garnet–tourmaline–muscovite leucogranites, and 5 = aplite.

5. Discussion

Li et al. (2013) divide Triassic post-ocean-closure granitoids across central Asia into two phases: (1) an Early to Middle Triassic (248–233 Ma) group that displays a large variation in $\epsilon\text{Nd}(t)$ values from -5.3 to $+5.8$ and TDM model ages from 0.99 Ga to 1.15 Ga and is interpreted to have been derived from a mixture of juvenile and ancient continental crust, and (2) a Late Triassic (230–204 Ma) group that is characterized by $\epsilon\text{Nd}(t)$ values from -2.3 to $+1.0$ and TDM model ages from 0.82 Ga to 1.21 Ga and inferred to have been derived mainly from juvenile crust (also see Li et al., 2014b). These authors further divide the Triassic central Asia igneous province sub-regions: the Altai belt, the North Mongolia–Transbaikalia belt, the central Mongolia–Erguna belt, the South Mongolia–Xing’an belt, the Beishan–Inner Mongolia–Jilin belt, and the northern margin of North China belt. In the scheme of Li et al. (2013), the Late Triassic plutonic complex examined in this study belongs to the second phase of Triassic igneous activities in the Altai belt. Based on the geochemistry and petrology of Late Triassic plutonic rocks in the Chinese Altai, Li et al. (2013) inferred that the late phase Triassic plutonism was induced by a mantle plume (see their Fig. 12).

In this study, we find that the biotite and two-mica granite was derived from a clay-poor source during vapor-absent melting at a higher temperature, whereas the coeval leucogranite was derived

from a clay-rich source during vapor-present melting at a lower temperature. The similarity in trace element composition between the schist exposed in the Bodonch metamorphic complex and the leucogranite hosted by the complex support the link that the schist was the protolith of the leucogranite.

Anatexis in the Mongolian Altai may be attributed to the following mechanisms: pressure-release melting induced by normal faulting (Harris and Massey, 1992) or locally focused erosion (Beaumont et al., 2001; Zeitler et al., 2001), flux melting during continental subduction (Le Fort et al., 1987), and shear (England et al., 1992; Harrison et al., 1998) and radiogenic (Huerta et al., 1998) heating during crustal thickening, and underplating of juvenile mafic magma during partial melting of the upper mantle (e.g., Li et al., 2013). Since our work is rather preliminary, the data collected from this study are insufficient to precisely pinpoint the mechanism of anatexis. Nevertheless, our work provides some general bounds on the potential geologic processes leading the emplacement of the observed granites.

Extension-induced pressure-release melting was proposed for the occurrence of the Himalayan leucogranites by Harris and Massey (1992). This model is based on the assumption that the South Tibet Detachment (STD) is a normal fault, a notion that is no longer valid in light of the recent geologic mapping that shows the STD merges with the Main Central Thrust acting as a passive roof thrust (Yin, 2006; Webb et al., 2007, 2011; Webb, 2013). In addition, the timing and petrology of the Himalayan leucogranites are also inconsistent with decompression melting (Harrison et al., 1998). In our study area, we found no evidence for the present of Triassic extensional faults that bound the Bodonch metamorphic complex, a structural requirement if the metamorphic complex is exhumed by extensional faulting. As such, we rule out the possibility that pressure release via normal faulting was the mechanism of Triassic crustal melting in the Mongolian Altai.

Focused erosion is commonly associated with collision-induced mountain building (Beaumont et al., 2001; Zeitler et al., 2001). As the Bodonch metamorphic complex is bounded by the Bulgan thrust, and the mutual cross-cutting relationships between the granites and shear-zone fabrics indicate coeval magmatism and thrusting were coeval, it is possible that focused erosion in the Bulgan thrust hanging wall caused pressure-release melting of the crustal material. Shear heating along the Bulgan thrust and accretion of radiogenic material in the footwall of the Bulgan thrust could also facilitate melting, as inferred for the occurrence of the Himalayan leucogranites (England et al., 1992; Harrison et al., 1998). Finally, the sediments thrust below the Bulgan thrust may have experienced dehydration and the release fluids (e.g., Le Fort et al., 1987) could further facilitate melting in the hanging wall of the Bulgan thrust.

Our inference that Late Triassic crustal melting and emplacement of granites in the Mongolia Altai occurred during crustal thickening is consistent with the regional constraints on the timing and kinematics of major faults in the Chinese Altai. There, the ages of a north-dipping thrust system with the Ertix thrust as the leading structure were determined by dating syn-kinematic monazite in the Ertix shear zone and the $^{40}\text{Ar}/^{39}\text{Ar}$ histories of the thrust hanging walls (Briggs et al., 2007, 2009). These efforts constrain the timing of the Chinese Altai thrust system, which is correlative along strike to the structures examined in this study, to have been active between 264 Ma and 160 Ma (Briggs et al., 2009). As the closure of the Paleo-Asia Ocean in the region occurred in the Late Carboniferous (Han et al., 2011) and locally in the earliest Permian (Zhang et al., 2012), thrusting in the Chinese Altai should have all occurred in an intracontinental setting along a convergence boundary between the Junggar Terrane and the Paleozoic Altai arc (Briggs et al., 2009).

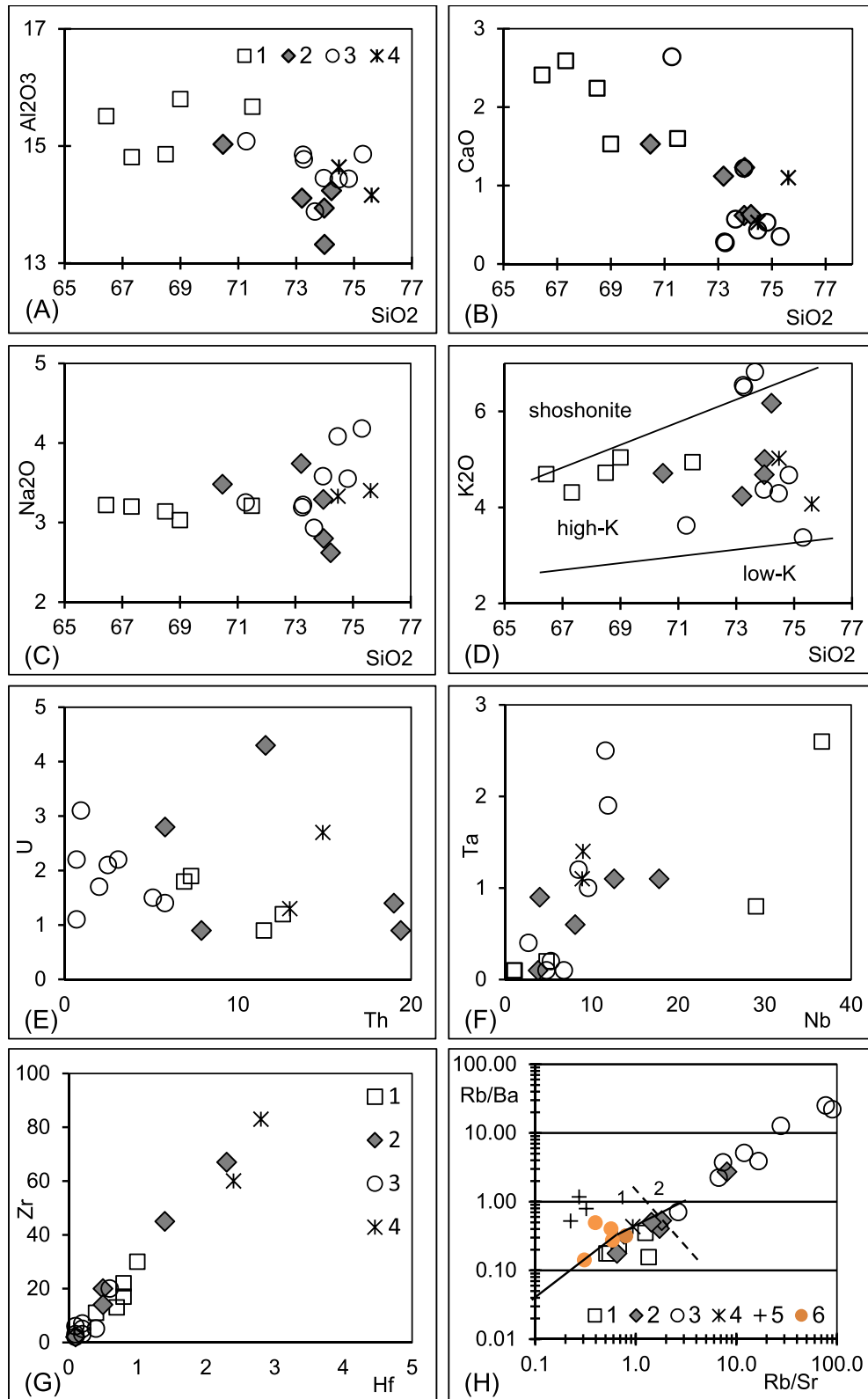


Fig. 6. (A–D) are Harker diagrams showing oxides against SiO₂ measured from our samples. (E) A U vs. Th plot with data points distinguishable between those from the leucogranite samples from the biotite granite, biotite–muscovite granite, and aplite samples. (F) A Ta vs. Nb plot with samples displaying an increasing trend of Ta with increasing Nb. (G) A Zr vs. Hf plot in which all samples show a positive linear correlation between Zr and Hf with a similar slope. (H) A Rb/Ba vs. Rb/Sr diagram. 1 = biotite granite, 2 = biotite–muscovite granite, 3 = garnet–muscovite, tourmaline–muscovite and garnet–tourmaline–muscovite leucogranites, 4 = aplites, 5 = paragneiss data from Jiang et al. (2012), 6 = schists and paragneiss of studied area. The boundary between series in K₂O–SiO₂ is from Rickwood (1989). Lines in Rb/Ba–Rb/Sr is from Sylvester (1998). 1 = clay poor, 2 = clay rich sources are divided by the dashed line.

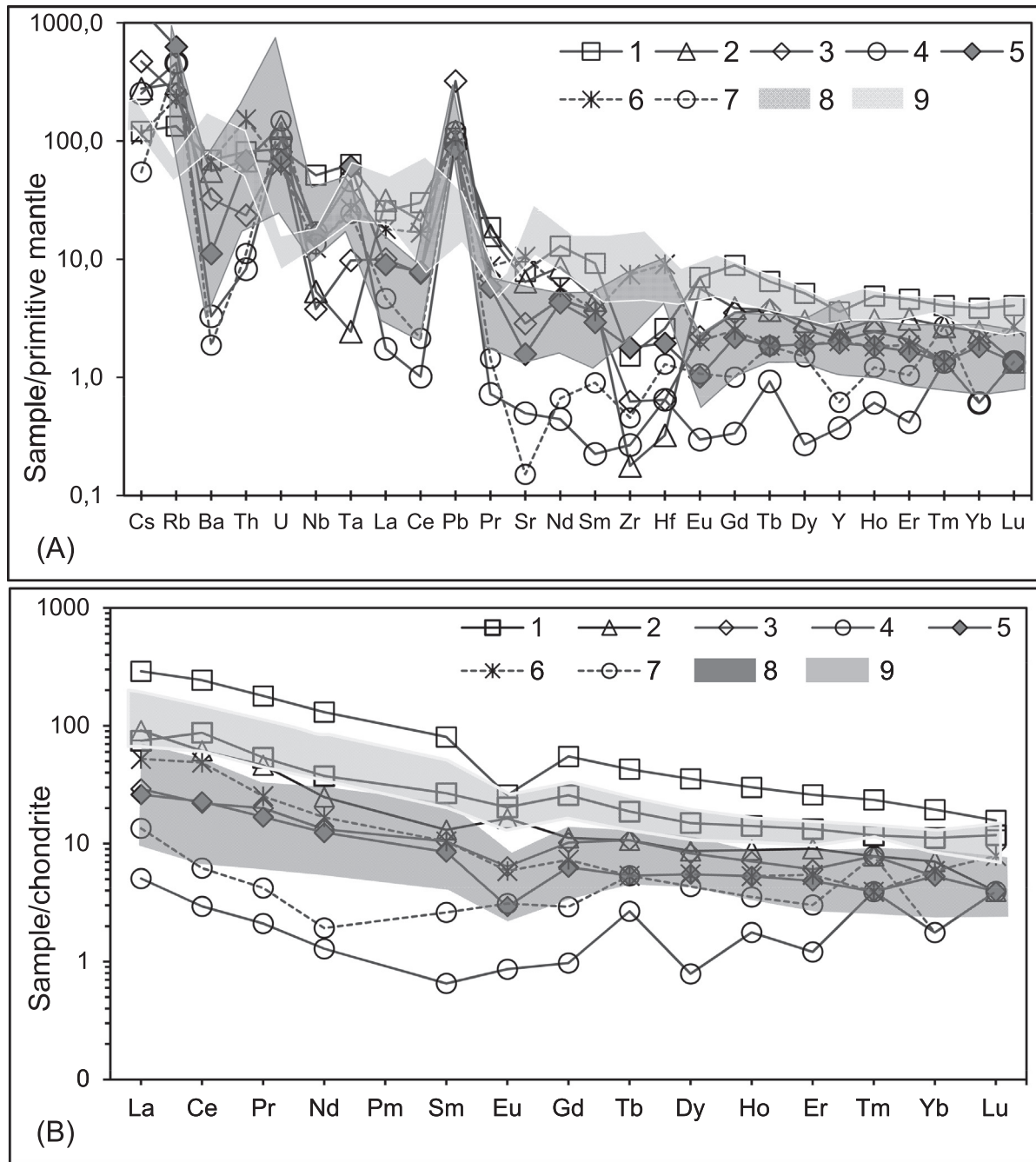


Fig. 7. (A) Primitive-mantle-normalized multi-element diagram. (B) Chondrite-normalized rare earth elements diagram. In both diagrams, samples 1–5 are samples collected along the banks of Bulgan River, where 1 = biotite granite; 2 = biotite–muscovite granite; 3 = tourmaline–muscovite leucogranite; 4 = garnet–muscovite–leucogranite; and 5 = garnet–tourmaline–muscovite leucogranite. Samples 6 and 7 are granite samples collected along the banks of Bodonch River, where 6 = aplite, 7 = garnet–muscovite–leucogranite; samples 8 and 9 in (A and B) are data from Himalayan garnet and biotite muscovite granite after Guo and Wilson (2012).

The inference of Late Triassic granites in the Mongolian Altai as anatexis is also consistent with their geochemical characteristics established from this study. According to Harris and Inger (1992), high concentrations of Rb and low concentrations of Ba and Sr indicate a fluid-absent melt source for the Himalayan leucogranites. Similar values of Rb, Ba, and Sr contents have been reported from trench sediments (Shimoda et al., 2003). Another characteristic of leucogranite is their high $^{87}\text{Sr}/^{86}\text{Sr}$ initial ratios. For example, the Himalayan leucogranites have a high initial Sr ratio of 0.7401–0.7620 (Deniel et al., 1987; Mukhopadhyay, 2001). In northwestern China, garnet-bearing leucogranites are characterized by Sr initial ratio of 0.706 and proposed partial melting from juvenile crust

(Wu et al., 2004). Generally the heterogeneous isotopic ratio of the leucogranites was explained by the isotopic heterogeneity of the source (Mukhopadhyay, 2001). Our samples show heterogeneous initial Sr ratios requiring melt sources from little recycled (Sr_i 0.7058 from biotite–muscovite granite) and highly recycled (Sr_i 0.5828 from garnet–muscovite granite) crust. The low Sr_i ratio of the biotite–muscovite granite may have been derived from a juvenile source or melting of mafic lower crust.

Paired Cenozoic leucogranite and biotite granites also occur in the Himalayan orogen, which are related to vapor-absent and vapor-present melting, respectively (e.g., Harrison et al., 1998). Both types of granites were related to shear heating along the Main



Fig. 8. CL images of zircon grains from a biotite–muscovite granite (sample number 62-09). Zircon zoning, dating spots, and corresponding U–Pb ages are also shown.

Central Thrust zone, as its motion was coeval with the emplacement of the granites. However, the Himalayan leucogranites were created in the up-dip segment of the Main Central Thrust where dehydration of subducted sediments released fluids to facilitate partial melting of the crust and thus the formation of the leucogranites (Harrison et al., 1998). In contrast, the biotite granite was formed by partial melting of dehydrated sediments subducted along the Main Central Thrust at a higher temperature (Harrison et al., 1998).

At a face value, the anatexis origin for the Mongolia Altai granites appears to be inconsistent with the inferences that Late Triassic granite in the Chinese Altai, which is located some 150–200 km west of our study area, was derived from a mantle source (e.g., the high-K Ala'er granite dated at ~210 Ma; Wang et al., 2014). However, this apparent discrepancy can be reconciled if the Late Triassic Chinese and Mongolian Altai granites were both induced by continental subduction that created two settings for the occurrence of granitic magmatism (Fig. 9). First, the high-K Ala'er-type

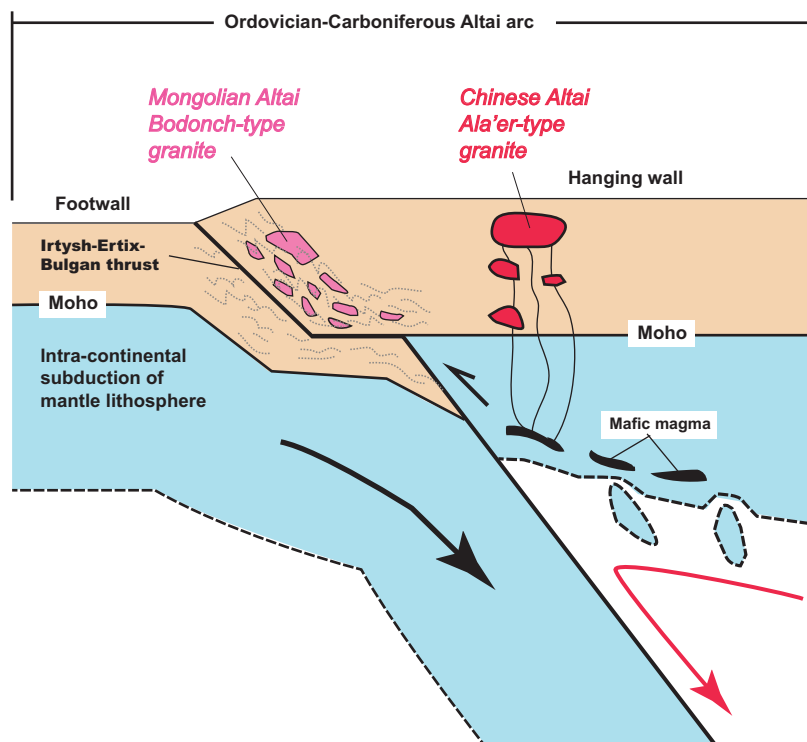


Fig. 9. Schematic tectonic model showing possible genesis of Late Triassic granites in the Altai region of central Asia.

granite was emplaced in regions where a thick mantle lithosphere was thinned by convective removal such as in Tibet as inferred by England and Houseman (1989). Alternatively, mantle melting could have been induced by continental subduction, a mechanism used to explain the occurrence of Cenozoic high-K magmatism in central Tibet (Tapponnier et al., 2001; Wang et al., 2001), slab tear leading to local rifting and basaltic underplating across an orogen (e.g., the Himalaya; see Yin, 2000). Second, the Bodonch-type granite was created along the intracontinental thrust zone (e.g., Bulgan thrust), where melting was induced by combined shear heating, radiogenic heating, flux melting, and decompression-induced melting through erosion (Fig. 9).

It is important to note that this work is highly preliminary due to the reconnaissance nature of the study. As such, several important problems remained unresolved. First, it remains unclear the total duration of granitic magmatism in the Mongolian Altai as a result of a lack of systematic dating of the igneous complex investigated in this study. Second, the timing of the Bulgan thrust shear zone in Mongolia is poorly known. The inferred coeval crustal thickening and magmatism is based on extrapolation of age constraints from the Chinese Altai, which may not be valid for the region in western Mongolia. Finally, our proposed continental subduction model via Late Triassic movement of the Irtysh–Ertix–Bulgan thrust system is highly speculative and requires detailed and integrated studies along different segments of this regionally significant structure.

6. Conclusions

In this study we document field relationships and geochemical characterization of a Late Triassic granitic complex in the western Mongolian Altai. The plutonic complex occurs as sills, dikes, and small stocks and its composition varies from biotite granite, two-mica granite, to leucogranite. Structurally, the plutonic complex occurs in the hanging wall of a segment of the regionally extensively (>1500 km long) Irtysh–Ertix–Bulgan thrust; the plutonic bodies both cut and are deformed by the shear fabrics in this regional thrust shear zone. The above relationship suggests that the duration of felsic magmatism and thrusting was temporally overlapping. Major and trace element data and isotopic analysis indicate that the felsic complex in our study area was derived from partial melting of meta-sediments, with the biotite and two-mica granite generated through vapor-absent partial melting and the leucogranite derived from flux melting. Although the Late Triassic granitic complex in the western Mongolian Altai is most likely originated from anatexis, the coeval granite in the Chinese Altai west of our study area in the hanging wall of the Irtysh–Ertix–Bulgan thrust was inferred by early studies to have been derived from mantle melting. In order to reconcile these seeming contradictory observations, we propose a Himalayan-style intracontinental-subduction model that predicts three settings for the occurrence of felsic magmatism: (1) along the intracontinental thrust zone where granite was entirely generated by anatexis as in the Mongolian Altai, and (2) in the hinterland region of the intracontinental thrust (i.e., the Irtysh–Ertix–Bulgan thrust) where convective removal and/or subduction of continental-mantle lithosphere may have induced mantle-derived melts as in the Chinese Altai.

Acknowledgments

We thank two very able anonymous reviewers for their critical and constructive comments. We also thank Prof. Wenjiao Xiao from the Chinese Academy of Sciences, Prof. N.B.W. Harris from Open University, Prof. Thomas K. Kelty from California State

University at Long Beach, and Dr. Pavel Hanzl from Czech Geological Survey for their comments and helpful suggestions that led to improvement of this paper. Finally, we would like to express our gratitude to the technical assistance from Dr. Masaaki Owada at Yamaguchi University of Japan for carrying out the XRF analysis. An Yin's work is supported by the China University of Geosciences (Beijing), SinoProbe administered by the Chinese Academy of Geological Sciences, and the US National Science Foundation.

References

- Aikman, A., Harrison, T.M., Hermann, J., 2012. The origin of Eo- and Neo-himalayan granitoids, Eastern Tibet. *J. Asian Earth Sci.* 58, 143–157.
- Badarch, G., Cunningham, W.D., Windley, B.F., 2002. A new terrane subdivision for Mongolia: implications for the Phanerozoic crustal growth of Central Asia. *J. Asian Earth Sci.* 21, 87–110.
- Barbarin, B., 1999. A review of the relationships between granitoid types, their origins and their geodynamic environments. *Lithos* 46, 605–626.
- Basu, A.R., Sharma, M., DeCellres, P.G., 1990. Nd, Sr-isotopic provenance and trace element geochemistry of Amazonian foreland basin fluvial sands, Bolivia and Peru: implications for ensialic Andean orogeny. *Earth Planet. Sci. Lett.* 100, 1–17.
- Beaumont, C., Jamieson, R.A., Nguyen, M.H., Lee, B., 2001. Himalayan tectonics explained by extrusion of a low-viscosity crustal channel coupled to focused surface denudation. *Nature* 414 (13), 738–742.
- Beresi, B., Trohopski, A., Don, E., 1964. Report of Geological Mapping at Scale of 1:200000 in Area of Uvs Province. Geological Survey of Mongolia, Ulaanbaatar.
- Briggs, S.M., Yin, A., Manning, C.E., Grove, M., Chen, Z.L., Wang, X.F., 2007. Late Paleozoic tectonic history of the Ertix Fault in the Chinese Altai and its implications for the development of the Central Asian Orogenic System. *Geol. Soc. Am. Bull.* 119, 771–784.
- Briggs, S.M., Yin, A., Manning, C.E., Chen, Z.L., Wang, X.F., 2009. Tectonic development of the southern Chinese Altai range as determined by structural geology, thermobarometry, $^{40}\text{Ar}/^{39}\text{Ar}$ thermochronology, and Th/Pb ion-microprobe monazite geochronology. *Geol. Soc. Am. Bull.* 121, 1381–1393.
- Chen, Bin, Jahn, B.M., 2002. Geochemical and isotopic studies of the sedimentary and granitic rocks of the Altai orogen of northwest China and their tectonic implications. *Geol. Mag.* 139, 1–13.
- Compton, W., Williams, I.S., Meyer, C., 1984. U–Pb geochronology of zircons from lunar Breccia 73217 using a sensitive high mass-resolution ion microprobe. *J. Geophys. Res.* 89, 525–534.
- Cunningham, W.D., 1998. Lithospheric controls on Late Cenozoic construction of the Mongolian Altai. *Tectonics* 17, 891–902. <http://dx.doi.org/10.1029/1998TC900001>.
- Cunningham, D., 2005. Active intracontinental transpressional mountain building in the Mongolian Altai: defining a new class of orogen. *Earth Planet. Sci. Lett.* 240, 436–444.
- Cunningham, W.D., Windley, B.F., Dorjnamjaa, D., Badamgarov, G., Saandar, M., 1996. A structural transect across the Mongolian Western Altai: active transpressional mountain building in central Asia. *Tectonics* 15, 142–156. <http://dx.doi.org/10.1029/95TC02354>.
- Cunningham, W.D., Windley, B.F., Owen, L.A., Barry, T., Dorjnamjaa, D., Badamgarov, J., 1997. Geometry and style of partitioned deformation within a late Cenozoic transpressional zone in the eastern Gobi Altai Mountains, Mongolia. *Tectonophysics* 277, 285–306.
- Cunningham, W.D., Davies, S.J., Badarch, G., 2003. Crustal architecture and active growth of the Sutaï Range, western Mongolia: a major intracontinental, intraplate restraining bend. *J. Geodynam.* 36, 169–191.
- De La Roche, H., Leterrier, J., Grandclaude, P., Marchal, M., 1980. A classification of volcanic and plutonic rocks using R1R2-diagram and major element analyses – its relationships with current nomenclature. *Chem. Geol.* 29, 183–210.
- Demin, A.D., 1990. Report of Project of Stratigraphy, Magmatism and Metallogeny Approach in Altai Province at Scale 1: 500 000. Geological Survey of Mongolia, Ulaanbaatar.
- Deniel, C., Vidal, P., Fernandez, A., Le Fort, P., Peucat, J.J., 1987. Isotopic study of the Manaslu granite (Himalaya, Nepal): inferences on the age and source of Himalayan leucogranites. *Contrib. Miner. Petrol.* 96, 78–92.
- England, P., Houseman, G., 1989. Extension during continental convergence, with application to the Tibetan plateau. *J. Geophys. Res.* 94, 17561–17579.
- England, P., Le Fort, P., Molnar, P., Pêcher, A., 1992. Heat sources for Tertiary metamorphism and anatexis in the Annapurna-Manaslu region, Central Nepal. *J. Geophys. Res.* 97, 2107–2128.
- Gansukh, D., Tileu, D., 1985. Report of Project on Geological Mapping at Scale of 1:200 000 in Area of Bayanulgi and Khovd Province. Geological Survey of Mongolia, Ulaanbaatar.
- Guo, Z.F., Wilson, M., 2012. The Himalayan leucogranites: constraints on the nature of their crustal source region and geodynamic setting. *Gondwana Res.* 22, 360–376.
- Han, B.F., Wang, S.G., Jahn, B.M., Hong, D.W., Kagami, H., Sun, Y.L., 1997. Depleted-mantle source for the Ulungur River A-type granites from North Xinjiang, China: geochemistry and Nd–Sr isotopic evidence, and implications for Phanerozoic crustal growth. *Chem. Geol.* 138, 135–159.

- Han, B.F., He, G.Q., Wang, X.C., Guo, Z.J., 2011. Late Carboniferous collision between the Tarim and Kazakhstan-Yiliterranes in the western segment of the South Tian Shan Orogen, Central Asia, and implications for the Northern Xinjiang, western China. *Earth Sci. Rev.* 109, 74–93.
- Harris, N.B.W., Inger, S., 1992. Geochemical characteristics of pelite-derived granites. *Contrib. Miner. Petrol.* 110, 46–56.
- Harris, N.B.W., Massey, J., 1994. Decompression and anatexis of the Himalayan metapelites. *Tectonics* 13, 1537–1546.
- Harris, N.B.W., Inger, S., Massey, J., 1993. The role of fluids in the formation of High Himalayan leucogranites. In: Treloar, P.J., Searle, M.P. (Eds.), *Himalayan Tectonics*. Geological Society London Special Publications, pp. 391–400.
- Harris, N.B.W., Ayres, M., Massey, J., 1995. Geochemistry of granitic melts produced during the incongruent melting of muscovite: implications for the extraction of Himalayan leucogranite magmas. *J. Geophys. Res.* 100, 767–777.
- Harrison, T.M., Grove, M., Lovera, O.M., Catlos, E.J., 1998. A model for the origin of Himalayan anatexis and inverted metamorphism. *J. Geophys. Res.* 103, 27017–27032.
- He, G., Han, B.F., Yue, Y., Wang, J., 1990. Tectonic division and crustal evolution of Altay Orogenic Belt in China. *Geosci. Xinjiang* 2, 9–20.
- Huerta, A.D., Royden, L.H., Hodges, K.V., 1998. The thermal structure of collisional orogens as a response to accretion, erosion, and radiogenic heating. *J. Geophys.* 15287–15302.
- Inger, S., Harris, N.B.W., 1993. Geochemical constraints on leucogranite magmatism in the Langtang Valley, Nepal Himalaya. *J. Petrol.* 34, 345–368.
- Jahn, B.M., Wu, F.Y., Chen, B., 2000. Granitoids of the Central Asian orogenic belt and growth of the continental crust in the Phanerozoic. *Trans. R. Soc. Edinburgh (Earth Sci.)* 91, 181–193.
- Kelty, T.K., Yin, A., Dash, B., Gehrels, G.E., Ribeiro, A.E., 2008. Detrital zircon geochronology of Paleozoic sedimentary rocks in the Hangay-Hentey basin, north central Mongolia: implications for the tectonic evolution of the Mongol-Okhotsk Ocean in central Asia. *Tectonophysics* 451, 290–311.
- Laurent-Charvet, S., Charvet, J., Monie, P., Shu, L.S., 2003. Late Paleozoic strike-slip shear zones in eastern central Asia (NW China): new structural and geochronological data. *Tectonics* 22 (2), 1009. <http://dx.doi.org/10.1029/2001TC901047>.
- Le Fort, P., Cuney, M., Deniel, C., France-Lanoë, C., Sheppard, S.M.F., Upreti, B.N., Vidal, P., 1987. Crustal generation of the Himalayan leucogranites. *Tectonophysics* 134, 39–57.
- Li, S., Wang, T., Wilde, S.A., Tong, Y., 2013. Evolution, source and tectonic significance of Early Mesozoic granitoid magmatism in the Central Asian Orogenic Belt (central segment). *Earth Sci. Rev.* 126, 206–234.
- Li, S.G., Wang, S.J., Guo, S.S., Xiao, Y.L., Liu, Y.C., Liu, S.A., He, Y.S., Liu, J.L., 2014a. Geochronology and geochemistry of leucogranites from the southeast margin of the North China Block: origin and migration. *Gondwana Res.* 26, 1111–1128.
- Li, S., Wilde, S.A., He, Z., Jiang, X., Liu, R., Zhao, L., 2014b. Triassic sedimentation and postaccretionary crustal evolution along the Solonker suture zone in Inner Mongolia, China. *Tectonics* 33, 2013TC003444.
- Lister, G.S., Snok, A.W., 1984. S-C mylonites. *J. Struct. Geol.* 6, 617–638.
- Maniar, P.D., Piccoli, P.M., 1989. Tectonic discriminations of granitoids. *Geol. Soc. Am. Bull.* 101, 635–643.
- Marinov, N.A. (Ed.), 1971. *Geological Map of Mongolian People's Republic at a Scale 1: 1500,000*. Nedra Press, Moscow.
- Marinov, N.A., Zonenshain, L.P., Blagoravov, V.A. (Eds.), 1973. *Geology of the Mongolian People's Republic. II. Magmatism, Metamorphism, Tectonics*. Nedra Press, Moscow, p. 750.
- Mukhopadhyay, D.K., 2001. Extreme heterogeneity in Sr isotope systematic in the Himalayan leucogranites: a possible mechanism of partial melting based on thermal modeling. *Proc. Indian Acad. Sci. (Earth Planet Sci.)* 110, 161–169.
- Plank, T., Langmuir, C.H., 1998. The chemical composition of subducting sediment and its consequences for the crust and mantle. *Chem. Geol.* 145 (3–4), 325–394.
- Polyanskii, O.P., Suhorukov, V.P., Travin, A.V., Alehin, I.G., Udin, D.S., 2011. Tectonic interpretation of thermochronological and *P-T* data of the Bodonch metamorphic complex. *Geol. Geophys.* 52, 1256–1275.
- Qu, G., Zhang, J., 1994. Oblique thrust systems in the Altay Orogen, China. *J. SE Asian Earth Sci.* 9, 277–287. [http://dx.doi.org/10.1016/0743-9547\(94\)90035-3](http://dx.doi.org/10.1016/0743-9547(94)90035-3).
- Ren, J., 2002. *Tectonic Map of Western China and Adjacent Regions at a Scale of 1:5,000,000*. Geological Publishing House, Beijing.
- Rickwood, P., 1989. Boundary lines within petrologic diagrams which use oxides of major and minor elements. *Lithos* 22, 247–263.
- Samozvantsev, B.A., Tsukeric, A.B., Golyakov, B.I., 1982. Report of Geological Mapping at a Scale of 1:200,000 from the Great Lakes Depression to the Western Branches of the Hangay Highland. Geological Survey of Mongolia, Ulaanbaatar (in Russian).
- Şengör, A.M.C., Natal'in, B.A., 1996. Paleotectonics of Asia: fragments of a synthesis. In: Yin, An, Harrison, T.M. (Eds.), *The Tectonic Evolution of Asia*. Cambridge University Press, pp. 486–640.
- Şengör, A.M.C., Natal'in, B.A., Burtman, V.S., 1993. Evolution of the Altaid tectonic collage and Paleozoic crustal growth in Eurasia. *Nature* 364, 299–307.
- Sepahi, A.A., Athari, S.F., Moazzen, M., 2007. Geochemistry and petrogenesis of the Tamuteh leucogranites in SW Saqqez, northwestern Iran. *Geochim. Cosmochim. Acta* 71, A917.
- Shimoda, G., Tatsumi, Y., Morishita, Y., 2003. Behavior of subducting sediments beneath an arc under a high geothermal gradient: constraints from the Miocene SW Japan arc. *Geochem. J.* 37, 503–518.
- Sola, A.M., Becchio, R.A., Pimentel, M.M., 2013. Petrogenesis of migmatites and leucogranites from Sierra de Molinos, Salta, Northwest Argentina: a petrologic and geochemical study. *Lithos* 177, 470–491.
- Stipska et al., 2010. Early Cambrian eclogites in SW Mongolia: evidence that the Palaeo-Asian Ocean suture extends further east than expected. *J. Metamor. Geol.* <http://dx.doi.org/10.1111/j.1525-1314.2010.00899.x>.
- Sylvester, J.P., 1998. Post-collisional strongly peraluminous granites. *Lithos* 45, 29–44.
- Sun, S.S., McDonough, W.F., 1989. Chemical and isotopic systematics of oceanic basalts: implications for mantle composition and processes. In: Saunders, A.D., Norry, M.J. (Eds.), *Magmatism in the Ocean Basins*. Geological Society of London, Special Publications 42, pp. 313–345.
- Tapponnier, P., Molnar, P., 1979. Active faulting and Cenozoic tectonics of Tien Shan, Mongolia, and Baikal regions. *J. Geophys. Res.* 84, 3425–3459.
- Tapponnier, P., Xu, Z.Q., Roger, F., Meyer, B., Arnaud, N., Wittlinger, G., Yang, J.S., 2001. Oblique stepwise rise and growth of the Tibet plateau. *Science* 294, 1671–1677.
- Tartese, R., Boulvais, P., 2010. Differentiation of peraluminous leucogranites “en route” to the surface. *Lithos* 114, 353–368.
- Wang, J.H., Yin, A., Harrison, T.M., Grove, M., Zhang, Y., Xie, G., 2001. A tectonic model for Cenozoic magmatism in the eastern Indo-Asian collision zone. *Earth Planet. Sci. Lett.* 188, 123–133.
- Wang, T., Jahn, B., Kovach, V.P., Tong, Y., Wilde, S., 2014. Mesozoic intraplate granitic magmatism in the Altai accretionary orogen, NW China: implications for the orogenic architecture and crustal growth. *Am. J. Sci.* 314, 1–42.
- Webb, A.A.G., Yin, A., Harrison, T.M., Célérier, J., Burgess, W.P., 2007. The leading edge of the Greater Himalayan Crystallines revealed in the NW Indian Himalaya: implications for the Evolution of the Himalayan Orogen. *Geology* 35, 955–958.
- Webb, A.A.G., 2013. Preliminary palinspastic reconstruction of Cenozoic deformation across the Himachal Himalaya (northwestern India). *Geosphere* 9, 572–587.
- Webb, A.A.G., Yin, A., Harrison, T.M., Célérier, J., Gehrels, G.E., Manning, C.E., Grove, M., 2011. Cenozoic tectonic history of the Himachal Himalaya (northwestern India) and its constraints on the formation mechanism of the Himalayan orogen. *Geosphere* 7, 1013–1061.
- Webb, A.A.G., Yin, A., Dubey, C.S., 2013. U–Pb zircon geochronology of major lithologic units in the Eastern Himalaya: implications for the origin and assembly of Himalayan rocks. *Geol. Soc. Am. Bull.* 125, 499–522.
- Windley, B.F., Kröner, A., Guo, J.H., Qu, G.S., Li, Y., Zhang, C., 2002. Neoproterozoic to Palaeozoic geology of the Altai orogen, NW China: new zircon age data and tectonic evolution. *J. Geol.* 110, 719–737.
- Windley, B.F., Alexeev, D., Xiao, W., Kröner, A., Badarch, G., 2007. Tectonic models for accretion of the Central Asian Orogenic Belt. *J. Geol. Soc.* 164, 31–47.
- Wu, F.-Y., Sun, D.-Y., Jahn, B.-M., Wilde, S., 2004. A Jurassic garnet-bearing granite pluton from NE China showing tetrad REE patterns. *J. Asian Earth Sci.* 23, 731–744.
- Xiao, W.J., Huang, B.C., Han, C.M., Sun, S., Li, J.L., 2010. A review of the western part of the Altai: a key to understanding the architecture of accretionary orogens. *Gondwana Res.* 18, 253–273.
- Yamasaki, T., Owada, M., Imaoka, T., Shiraki, K., 1999. Major and trace element analyses of rock samples by X-ray fluorescence spectrometry. *Tech. Rep. Center Instrum. Analyses* 7, 22–31.
- Yanshin, L.A. (Ed.), 1978. *Tectonic Map of Mongolian People's Republic at a Scale 1 to 1500,000*. Nedra Press, Moscow.
- Yanshin, L.A. (Ed.), 1989. *Geological Formations Map of Mongolian People's Republic at a Scale of 1:1500 000*. Nedra Press, Moscow.
- Yang, X., Xie, G., Li, Z., 1992. Mylonite–migmatite lithogenic series – an important tectono-dynamic rock forming process. *Geotect. Metall.* 16, 151–159.
- Yin, A., 2000. Mode of Cenozoic east–west extension in Tibet suggesting a common origin of rifts in Asia during the Indo-Asian collision. *J. Geophys. Res.* 105, 21745–21759.
- Yin, A., 2006. Cenozoic tectonic evolution of the Himalayan orogen as constrained by along-strike variation of structural geometry, exhumation history, and foreland sedimentation. *Earth-Sci. Rev.* 76, 1–131.
- Yin, A., Harrison, T.M., 2000. Geological evolution of the Himalayan-Tibetan orogen. *Annu. Rev. Earth Planet. Sci.* 28, 211–280.
- Zeitler et al., 2001. Crustal reworking at Nanga Parbat, Pakistan: metamorphic consequences of thermal–mechanical coupling facilitated by erosion. *Tectonics* 20, 712–728.
- Zhang, C.L., Santosh, M., Zou, H.B., Xu, Y.G., Zhou, G., Dong, Y.G., Ding, R.F., Wang, H. Y., 2012. Revisiting the “Irtish tectonic belt”: implications for the Paleozoic tectonic evolution of the Altai orogen. *J. Asian Earth Sci.* 52, 117–133.
- Zorigtkhuu, O., Tsunogae, T., Dash, B., 2011. Metamorphic *P-T* evolution of garnet–kyanite–staurolite schist and garnet amphibolite from Bodonch area, western Mongolian Altai: geothermobarometry and mineral equilibrium modeling. *J. Asian Earth Sci.* 42, 306–315.
- Zorigtkhuu, O., Tsunogae, T., Dash, B., 2012. Carbonic fluid inclusions in amphibolite-facies pelitic schists from Bodonch area, western Mongolian Altai. *J. Mineral. Petrol. Sci.* 107, 44–49.